

Super-resolving Compressed Images via Parallel and Series Integration of Artifact Reduction and Resolution Enhancement

Hongming Luo, Fei Zhou, Guangsen Liao, and Guoping Qiu

Abstract—In real-world applications, images may be not only sub-sampled but also heavily compressed thus often containing various artifacts. Simple methods for enhancing the resolution of such images will exacerbate the artifacts, rendering them visually objectionable. In spite of its high practical values, super-resolving compressed images is not well studied in the literature. In this paper, we propose a novel compressed image super resolution (CISR) framework based on parallel and series integration of artifact removal and resolution enhancement. Based on maximum a posterior inference for estimating a clean low-resolution (LR) input image and a clean high resolution (HR) output image from down-sampled and compressed observations, we have designed a CISR architecture consisting of two deep neural network modules: the artifact reduction module (ARM) and resolution enhancement module (REM). ARM and REM work in parallel with both taking the compressed LR image as their inputs, while they also work in series with REM taking the output of ARM as one of its inputs and ARM taking the output of REM as its other input. A unique property of our CSIR system is that a single trained model is able to super-resolve LR images compressed by different methods to various qualities. This is achieved by exploiting deep neural networks capacity for handling image degradations, and the parallel and series connections between ARM and REM to reduce the dependency on specific degradations. ARM and REM are trained simultaneously by the deep unfolding technique. Experiments are conducted on a mixture of JPEG and WebP compressed images without a priori knowledge of the compression type and compression factor. Visual and quantitative comparisons demonstrate the superiority of our method over state-of-the-art super resolution methods, especially for heavily compressed images. Ablation studies are also conducted to show the impacts of different parts in the proposed model.

Index Terms—Artifact reduction, Compressed image, parallel and series integration, super resolution.

I. INTRODUCTION

SINGLE image super resolution (SR) aims to reconstruct a high-resolution (HR) image from its low-resolution (LR)

counterpart [1]. It has received much attention due to its values in many applications, such as surveillance imaging [2], [3] and thumbnail image enlargement [4]. In almost all practical applications, limited by storage capacity and transmission bandwidth, images are not only down-scaled but also compressed. If the compression is lossy, LR images are inevitably contaminated by annoying artifacts, such as blocking, ringing, blurring, fake edges, etc. Enhancing the resolution of such images will exacerbate the artifacts. Thus, in comparison to clean images, it is more challenging to super-resolve compressed images, especially heavily compressed ones. Despite its practical application values, compressed image super resolution (CISR) is not well studied in the literature, and there are many problems remain unsolved. This work focuses on the single image SR (SISR) problem for compressed images.

Many SISR methods have been developed in the literature. Some methods perform an adaptive interpolation to enlarge the LR input [5], [6], [7], while some other methods aim to design image priors in a regularization framework [8], [9], [10]. Some methods adopt a shallow regression to relate the input and the HR output [11], [12], [13], while recent methods map LR images to HR ones by making use of deep neural networks [14], [15], [16]. Most of existing SISR methods assume a clean LR image as the input, which only suffers from aliasing. However, a real LR image would suffer from more complex degradations, e.g., compression. The recent testing in [17] demonstrates that most SISR methods fail to process real-world LR images. Some researchers have been aware of this problem in their SISR researches and attempted to super-resolve images with different degradations. Among various degradations, additive noises and blurring are most considered in the SISR literature [18], [19]. However, compression-induced artifacts are totally different from additive noises and blurring. First, additive noises are independent from image contents, and the noise distribution generally remains the same over the whole image. In contrast to additive noises, compression artifacts would be highly related to image contents and spatially variant. Second, blurring kernels can be spatially variant but produce no high-frequency artifact. Different from blurring, compressions could give rise to high-frequency artifacts, e.g., blocking.

To super-resolve compressed images, a straightforward idea is to involve compressions in preparing the training data and employ a commonly-used SISR model to directly relate compressed LR images and clean HR ones. However, such simple strategy can hardly produce high-quality super-resolved images

This work was in part supported by the Education Department of Guangdong Province, China with No. 2019KZDZX1028, and in part by the Initial Funding of Newly-Introduced Teacher in Shenzhen University with No. 2019121.

The authors are with the College of Electronic and Information Engineering, Shenzhen University, Shenzhen 518060, China (e-mail: lh0220@qq.com; flying.zhou@163.com; liao Guangsen2018@email.szu.edu.cn; qiu@szu.edu.cn).

G. Qiu is also with the School of Computer Science, University of Nottingham, Nottingham, U.K. (e-mail: guoping.qiu@nottingham.ac.uk).

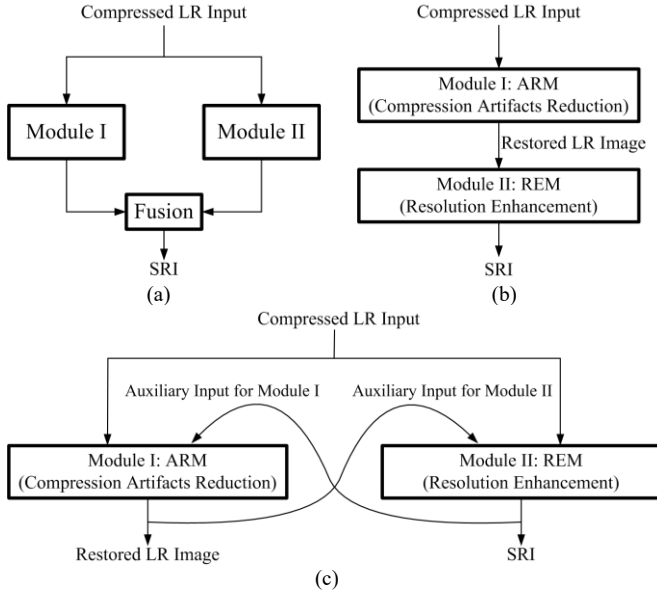


Fig. 1. Illustrations on different frameworks for CISR. (a) Parallel framework. (b) Series or cascaded framework. (c) Our framework.

(SRIs). The underlying reason is that, with the enhancement of the primitive signals of image content, some high-frequency artifacts would be incorrectly enlarged [20]. In previous work, several specific models have been designed for CISR. Their frameworks fall into two categories: joint model [21], [22] and series (or cascaded) model [23], [24]. Specifically, the joint model is a parallel architecture, where the input image or part of it streams to two independent modules simultaneously, and the results from the two modules are fused to obtain the output, as shown in Fig. 1(a). In [21], one module super-resolves patches without blocking, while the other module processes blocking patches. In [22], one module directly enlarges the input image, and the other module super-resolves a de-noised version of the input. However, two independent modules cannot benefit each other, limiting the performance of SISR for compressed images. In series or cascaded models, the output of one module streams to the next module. Generally, two modules are involved at least: one is the artifact reduction module (ARM) and the other one is for resolution enhancement. If the resolution enhancement module (REM) is applied first, some artifacts would be enhanced. It is much more difficult to suppress the enhanced artifacts than the original ones. Therefore, in existing methods [20], [23], [24], the LR input image is first restored by reducing compression artifacts and then rescaled to a higher resolution, as shown in Fig. 1(b). Nevertheless, some image details would be inevitably lost during the artifact reduction, and those lost details can hardly be retrieved by subsequent modules.

Different from previous work, our framework of the proposed model is illustrated in Fig. 1(c). Our system is designed based on maximum a posterior (MAP) inference for estimating a clean version of the LR input image and a clean version of the HR output image from down-sampled and compressed observations. Formal descriptions of the derivation of our model design will be presented in Section III.A. A benefit of our system is that a single trained model is able to super-resolve LR images compressed by different methods to various qualities. It

is achieved through exploiting deep neural networks capacity for handling image degradations and using auxiliary inputs to reduce the dependence on specific degradations.

In Fig. 1(c), there also exist two modules: ARM (Module I) and REM (Module II). However, these two modules are not simply parallel or cascaded. On one hand, the compressed LR input streams to two modules in a parallel way. On the other hand, the output of one module is fed back to the other module, resulting in two series flows. Here, we regard the output of one module as the auxiliary input of the other one. Essentially, both parallel and series flows are involved in our framework. Its advantages are threefold: First, original information in the input is fully available to both modules. Second, the output of Module I facilitates Module II by providing a relatively clean version of the LR image. Third, the output of Module II supplies Module I with high-frequency image details, which is frequently lost during the artifact reduction.

In this work, both modules are implemented by deep neural networks, and the training is achieved by the deep unfolding technique [25]. In addition, at the beginning of each module, we include a non-local operator to capture long-range dependencies in images. In an SISR deep network, a long skip connection has been demonstrated to be highly effective in forcing the network to learn residuals, i.e., high-frequency image details [28]. It not only allows most low-frequency information to take a shortcut, but also alleviates the problem of vanishing or exploding gradients [29]. Hence, a long skip connection is also adopted in each module of our framework. Since three images, i.e., the input, the auxiliary input, and the non-locally filtered image, are available, we propose to adaptively combine them for the skip connection by learning their respective weights during the network training. That is, all the three images are connected to the output but with learnable contributions.

The rest of the paper is organized as follows. In Section II, we briefly review some related work. Section III describes the proposed CISR method in detail. The experiments are provided in Section IV. Conclusions are drawn in Section V.

II. RELATED WORK

In this section, we will first review some related techniques used in the SISR methods that are designed for clean LR images. Then, SISR methods for the LR images with various degradations are investigated. Finally, we would like to include some well-known methods for compression artifacts reduction.

A. Super Resolution for Clean Images

Early models in SISR are example-based [30], [31], where a search for the nearest neighbor is performed with compatibility constraints. Subsequent famous methods include the models based on locally linear embedding [32], based on sparse coding [9], based on neighborhood regression [12], etc. In spite of various techniques, all of them, called traditional methods, are limited by their shallow architectures. One can refer to [1] for the detailed review of traditional SISR methods.

The emergence of deep learning techniques further enriched SISR researches. In [14], a convolutional neural network with two hidden layers is exploited to imitate the procedures in

traditional SISR methods. In [33], the principle of sparse coding is absorbed into deep learning by using a sub-network to imitate the learned iterative shrinkage and thresholding algorithm (LISTA). The first few attempts in [14], [33] successfully adopts deep networks in SISR tasks. However, they fail to build much deeper networks which are believed to be more powerful. To achieve a very deep network, the method in [28] employs a long skip connection to pass the interpolated LR image to the output, known as global residual learning. Moreover, the model of enhanced deep super-resolution network (EDSR) utilizes stacked residual blocks [34], known as local residual learning. Some models utilize more complex residual learning to deliver information from previous layers to subsequent ones, such as persistent memory network [35] and residual dense network [36]. In addition to residual learning, the deep back-projection network uses iterative up- and down-projection units to correct propagation errors [37]. As networks go deeper, it is important to fully exploit their representational ability. For this purpose, interdependencies among channels are considered in the residual channel attention network (RCAN) [38]. It includes multiple residual groups, each of which further contains multiple channel attention blocks. The SISR model of second-order attention network (SAN) can be found in [39], where second-order interdependencies are considered. One can refer to [15] and [16] for comprehensive surveys of deep SISR models.

In some deep SISR models [40], [41], recursive learning has been demonstrated to be very effective on stabilizing training and preventing the number of learnable parameters from a steep increase. A recursion of multiple convolution layers is used in [40], while a recursive block of several residual units is introduced in [41]. In essence, the recursion of layers or units can be regarded as a recurrent network [42] or a feedback network [43]. A dual-state recurrent network is proposed in [42] by providing information streams from LR to LR, HR to HR, and LR to HR features, respectively. In [43], a feedback block with dense skip connections is presented to transmit high-level information back to a low-level layer. In these methods, deep networks are unfolded to make their training feasible [42], [43]. The success of unfolding technique in deep SISR models motivates us to employ it to train our model in Fig. 1(c), where the auxiliary inputs can be treated as feedback information.

Moreover, non-local means has been successfully adopted in both traditional and deep SISR methods. In [44], a regularization of non-local regression is embedded in the SISR framework of sparse coding. In [45], a non-local total variation prior is incorporated with an adaptive geometric duality prior to infer HR images. The model in [46] extends the model in [45] by shifting target patches in the search of non-local similar patches. In deep SISR models, non-local means is known as the spatial attention that is essentially a non-local convolution process. In [47], the authors combine the idea of iterative projections in [37] with two kinds of attention blocks. One kind of attention block is based on the features from the same layer, and the other one is based on feature correlations cross different levels. The SISR method in [48] incorporates channel attention modules in [38] with spatial attention modules to improve the network representation ability on interest regions.

Albeit great success of the above methods for clean images, they fail to super-resolve compressed images. The deep models with excellent performance on clean images are just comparable or even inferior to some traditional methods on the images that suffer from real-world degradations [17]. This phenomenon is known as simulated-to-real gap.

B. Super Resolution for Images with Various Degradations

In real-world cases, images may suffer from not only aliasing but also other degradations. To reduce the simulated-to-real gap, some SISR methods are developed for the images with various degradations. Among these methods, LR images with noises and blurring are often investigated, and only a small number of methods focus on compressed images. In this sub-section, we would like to briefly review these methods.

To super-resolve noisy LR images, a convex combination of a noisy SR image and a de-noised SR image is used in [18] to infer the final SR result under three kinds of constraints. In [49], a de-noising procedure is performed at a middle resolution between LR and HR to prevent the residual noises from being boosted. In [50], the noise level of LR images is first estimated and then employed to determine the value of regularization parameter. Recently, the noise-robust iterative back-projection (NRIBP) is presented in [51] for noisy image SR. It minimizes the cost function that is an adaptive combination of noisy and de-noised SR reconstruction errors in the transform domain of principal component analysis. Essentially, most methods for noisy image SR take advantage of the independence between image content and noises.

In addition to noises, some models further consider the impact of various blur kernels in SISR. In [52], blur kernel and noise level are regarded as one channel of the input via a dimensional stretching strategy, making deep networks possible to handle blurring and noises. In [53], an auxiliary variable is introduced to separate the problem of blurred image SR to two iterative sub-problems. One is an image restoration problem, which has a closed-form solution in the Fourier domain. The other one is an SR problem for a given noise level, which can be achieved by embedding an already-trained super-resolver. To handle the images with spatially variant blur kernels, a kernel prediction network is employed in [19] to estimate pixel-wise up-sampling kernels in a multi-scale fashion. Inspired by the SISR model based on generative adversarial networks [54], the strategy in [55] is to transfer the input noisy and blurred images to the distribution of clean LR images in an unsupervised way. Recently, a meta-upscale layer is introduced in [56] to adaptively relate LR features and the output according to three degradation parameters, including scale factor, blur kernel, and noise level. These degradation parameters are also considered in the model of unfolding super-resolution network (USRNet) [57], which extends the work in [53] by introducing a trainable prior module. However, it is required that degradation parameters are available in most methods mentioned above, e.g., [52], [53], [56], [57]. Moreover, the models designed for noisy and blurred images are not appropriate for compressed images, as we will demonstrate in Section IV.B.

In comparison with noisy and blurred image SR, studies on

the SISR problem for compressed images are relatively seldom. The method in [20] first performs an iterative restoration procedure, where regularization strength is controlled based on the observation on energy change characteristics of primitive and non-primitive signals. Then, SR is achieved via a pair matching strategy. However, some image details are inevitably lost during the restoration procedure. In [21], patches are classified into two sets of blocking and non-blocking ones by a blocking detection algorithm. Non-blocking patches are super-resolved via a sparse coding paradigm, and the process of blocking patches is treated as the image decomposition problem based on morphological component analysis. Regarding compression artifacts as noises, the method in [22] adopts a similar strategy in [18], i.e., fusing a noisy result and a de-noised one to produce the final result. However, the methods in [20]–[22] ignore the information exchange between different modules. The model of iterative cascaded SR and de-blocking (ICSD) [23] is the first attempt to use the information exchange between de-blocking and SR. Specifically, a down-scaled high-frequency part of SRI is utilized to constrain the de-blocking. Nevertheless, as traditional methods, the above methods are limited by their shallow architectures and empirical selections of model parameters. In [24], CISR is implemented by deep convolution neural networks (CISRDCNN), which consists of three cascaded modules. In addition to a de-blocking module followed by an up-sampling module, a supplementary module is added at the end to enhance images. The three modules are trained individually at first, and then are jointly optimized. However, the details lost in previous modules can hardly be retrieved by subsequent ones. Moreover, the information exchange among different modules is not fully exploited.

C. Compression Artifacts Reduction

As this work focuses on compressed images, the techniques of compression artifacts reduction are related to this work. Here, we would like to briefly review some of these techniques.

Traditional methods are mainly dedicated to the reduction of blocking artifacts, which are most visually annoying. They can be performed in either spatial domain [58], [59] or transform domain [60], [61]. The algorithm in [58] processes compressed images in a pixel-by-pixel way to identify and reduce blocking artifacts. In [59], compression artifacts are modeled as additive, spatially correlated Gaussian noise, while the image content is modeled by a Markov random field. In [60], blocking artifacts are first detected in the discrete cosine transform (DCT) domain, and then reduce the artifacts by correcting DCT coefficients. The method of shape-adaptive DCT (SA-DCT) [61] defines the shape of the transform support in a pointwise adaptive way to produce clean edges. Similar to the development of SISR, deep learning has also achieved success in the field of compression artifacts reduction recently. Inspired by [14], the model in [62] achieve compression artifacts reduction via a three-layer convolutional network, where a feature enhancement layer is included to map noisy features to clean ones. To take advantage of both spatial and transform domains, some methods exploit deep dual-domain models [63], [64]. The modules for spatial and transform domains can be either parallel [63] or cascaded

[64]. The de-noising convolutional neural network (DnCNN) model is presented in [65], which implicitly removes the latent clean image with the help of residual learning. The method in [66] uses an auto-encoder architecture as the backbone, where a deep classifier is further included to estimate coefficient distributions in the frequency domain. Recently, the deep convolutional sparse coding (DCSC) [67] is proposed to achieve compression artifacts reduction by multi-scale feature extractors and convolutional LISTA. One can refer to [68] for the detailed review of studies on compression artifacts reduction.

It would be interesting to see that many techniques or models have been successfully applied to both the problems of SISR and compression artifacts reduction. For example, the trainable nonlinear reaction diffusion (TNRD) model can be trained with different reaction terms to solve the two problems [69]. As a well-known technique in SISR, sparse coding is also introduced for compression artifacts reduction in either traditional methods [70] or deep models [67]. Furthermore, the non-local means [71] and attention networks [72] are employed to reduce compression artifacts. This phenomenon can be attributed to the common properties of reproduced images and learning models.

III. PROPOSED SISR MODEL FOR COMPRESSED IMAGES

A. Formulation

For a compressed LR image \mathbf{z} , it suffers from two degradations at least. The first degradation is known as aliasing, which is attributed to a discrete sampling procedure, such as image acquisition. The second one is the compression-induced artifacts, which would appear in transmission and storage procedures. Thus, it is reasonable to assume that the down-sampling procedure is followed by the compression procedure [20]–[24]. By considering the sub-sampling procedure, a clean LR image \mathbf{y} can be obtained from its HR counterpart \mathbf{x} via a MAP inference:

$$\mathbf{y} = \arg \min_{\mathbf{y}} \|\mathbf{y} - \mathbf{D}\mathbf{x}\|^2 + \lambda_1 \psi(\mathbf{y}), \quad (1)$$

where \mathbf{D} is a down-sampling operator, $\psi(\mathbf{y})$ is the regularization term describing the prior knowledge of \mathbf{y} , and λ_1 is a parameter to balance the two terms in (1). Furthermore, we can estimate the clean LR image \mathbf{y} from its compressed counterpart \mathbf{z} by

$$\mathbf{y} = \arg \min_{\mathbf{y}} \|\mathbf{T}^{-1}\mathbf{Q}\mathbf{T}\mathbf{y} - \mathbf{z}\|^2 + \lambda_2 \psi(\mathbf{y}), \quad (2)$$

where λ_2 is a trade-off parameter, \mathbf{T} is a linear transform used in compression, \mathbf{T}^{-1} is the corresponding inverse transform, and \mathbf{Q} is a quantization operator. In this work, we do not assume any specific transform, although the discrete cosine transform is widely used in compressing images by following the JPEG standard [73]. Here, we investigate the sampling and compression procedures respectively. Thus, the data fidelity terms in (1) and (2) are different. In contrast, the regularization terms remain unchanged, as the prior knowledge of clean LR images is the same. Considering both the procedures of down-sampling and compression, we can aggregate (1) and (2) to get

$$\mathbf{y} = \arg \min_{\mathbf{y}} \|\mathbf{y} - \mathbf{D}\mathbf{x}\|^2 + \alpha \|\mathbf{C}\mathbf{y} - \mathbf{z}\|^2 + \lambda \psi(\mathbf{y}), \quad (3)$$

where $\mathbf{C} = \mathbf{T}^{-1}\mathbf{Q}\mathbf{T}$ represents the compression process, α and λ are trade-off parameters. In the context of down-sampling and compression, the formula in (3) implies that both the HR image \mathbf{x} and the compressed LR image \mathbf{z} contribute to the estimation of the clean LR image \mathbf{y} . In the problem of super-resolving compressed image, only the compressed LR image \mathbf{z} is available. For the unknown HR image \mathbf{x} , we can use its estimation, i.e., SRI, as an alternative.

Our final purpose is to produce the HR image \mathbf{x} instead of \mathbf{y} , although it is intuitive that the recovery of a clean LR image is beneficial. In the SISR paradigm, given a clean LR image \mathbf{y} , its HR counterpart is obtained by

$$\mathbf{x} = \arg \min_{\mathbf{x}} \|\mathbf{D}\mathbf{x} - \mathbf{y}\|^2 + \mu_1 \phi(\mathbf{x}), \quad (4)$$

where μ_1 is a balance parameter, and $\phi(\mathbf{x})$ is the regularization term describing the prior knowledge of \mathbf{x} . Unfortunately, the clean LR image is not available when we super-resolve compressed images. It is straightforward to estimate \mathbf{y} first by using (2). However, as we mentioned in Section I and II.B, the estimation on \mathbf{y} cannot be perfect. That is, some intrinsic contents in \mathbf{z} are inevitably lost when producing \mathbf{y} . Therefore, we further include the following MAP estimation

$$\mathbf{x} = \arg \min_{\mathbf{x}} \|\mathbf{C}\mathbf{D}\mathbf{x} - \mathbf{z}\|^2 + \mu_2 \phi(\mathbf{x}), \quad (5)$$

where μ_2 is a balance parameter. Since the prior knowledge of \mathbf{x} is also the same, we use the same regularization term for both (4) and (5). Similar to (3), we can estimate \mathbf{x} by linearly combining (4) and (5):

$$\mathbf{x} = \arg \min_{\mathbf{x}} \|\mathbf{D}\mathbf{x} - \mathbf{y}\|^2 + \beta \|\mathbf{C}\mathbf{D}\mathbf{x} - \mathbf{z}\|^2 + \mu \phi(\mathbf{x}), \quad (6)$$

where β and μ are trade-off parameters. By (6), it is clear that both \mathbf{y} and \mathbf{z} are required in estimating the HR image \mathbf{x} . Similarly, for the unknown clean LR image \mathbf{y} , we can use its estimation, i.e., restored LR image, as an alternative.

In the proposed framework shown in Fig. 1(c), the ARM, i.e., Module I, aims to achieve the optimization in (3). Meanwhile, the REM, i.e., Module II, is associated with (6). That is, the ARM outputs an estimation of \mathbf{y} , and the REM generates an estimation of \mathbf{x} . According to (3), in addition to the compressed LR image \mathbf{z} , the output of Module II should be fed back into Module I. We call it the auxiliary input to Module I, as shown in Fig. 1(c). Similarly, according to (6), the output of Module I serves as the auxiliary input to Module II. With the input \mathbf{z} and the auxiliary input, both parallel and series streams are included in the proposed framework. The parallel stream is from the compressed LR image \mathbf{z} to the output of each module. Besides, there are two series flows: one is from Module I to Module II, and the other one is from Module II back to Module I.

As pointed out in [74], an MAP-based inference can be replaced by a plain discriminative learning, which learns a direct mapping to model image prior implicitly rather than explicitly. Therefore, the solution to (3) can be given by

$$\mathbf{y} = \mathcal{P}(\mathbf{x}, \mathbf{z}; \Theta_1), \quad (7)$$

where $\mathcal{P}(\cdot)$ denotes the mapping for Module I, and Θ_1 represents the parameters in \mathcal{P} . In this work, the mapping \mathcal{P} is implemented by a deep neural network, details of which will be described in the next sub-section. Strictly speaking, in (7), we should also include degradation parameters as the inputs of \mathcal{P} , as formulated in [53] and [57]. In our case, the most important degradation parameters are the ones related to compression quality. In JPEG compression, for example, we can utilize the quantization table. However, the inclusion of such degradation parameters would limit our model to some specific compression. Very importantly, we aim to design a single model which is able to super-resolve LR images compressed by different methods to various qualities. We achieve this by exploiting the capacity of deep neural networks for handling images with various levels of degradation levels [65] and the auxiliary inputs which can largely reduce the dependence of \mathcal{P} on specific degradations. Thus, we do not include any degradation parameters in (7), resulting in a blind restoration process. In the same manner, we can rewrite (6) by

$$\mathbf{x} = \mathcal{R}(\mathbf{y}, \mathbf{z}; \Theta_2), \quad (8)$$

where $\mathcal{R}(\cdot)$ denotes the mapping for REM, and Θ_2 represents the parameters in \mathcal{R} .

B. Architectures of Modules I and II

In this sub-section, we will detail the mappings $\mathcal{P}(\cdot)$ and $\mathcal{R}(\cdot)$, which are implemented via deep networks. The mapping $\mathcal{P}(\cdot)$ in (7) essentially achieves artifact reduction, and the mapping $\mathcal{R}(\cdot)$ in (8) is used for the resolution enhancement. As mentioned in Section II.C, the solutions to these two problems share many common techniques and models. Therefore, we employ similar architectures for both mappings, as illustrated in Fig. 2. Most recently-developed architectures and related techniques can be used to embody ARM and REM. In this work, we adopt several residual groups of RCAN [38] as the backbone of these two modules. Moreover, in each module, we include a non-local operator, highlighted in cyan in Fig. 2. The non-local operator can benefit both the mappings in (7) and (8) by capturing long-range dependencies over the whole image. Different from previous non-local operators that only operate on the input image, we make use of both the input and the auxiliary input to weaken the influence of blocking artifacts. After the non-local operator, its output, the input, and the auxiliary input are concatenated for subsequent processing. In addition to skip connections in the backbone, a long skip connection, marked in blue in Fig. 2, is used to pass the concatenated images to the output by a shortcut. Thereinto, an adaptive combination of

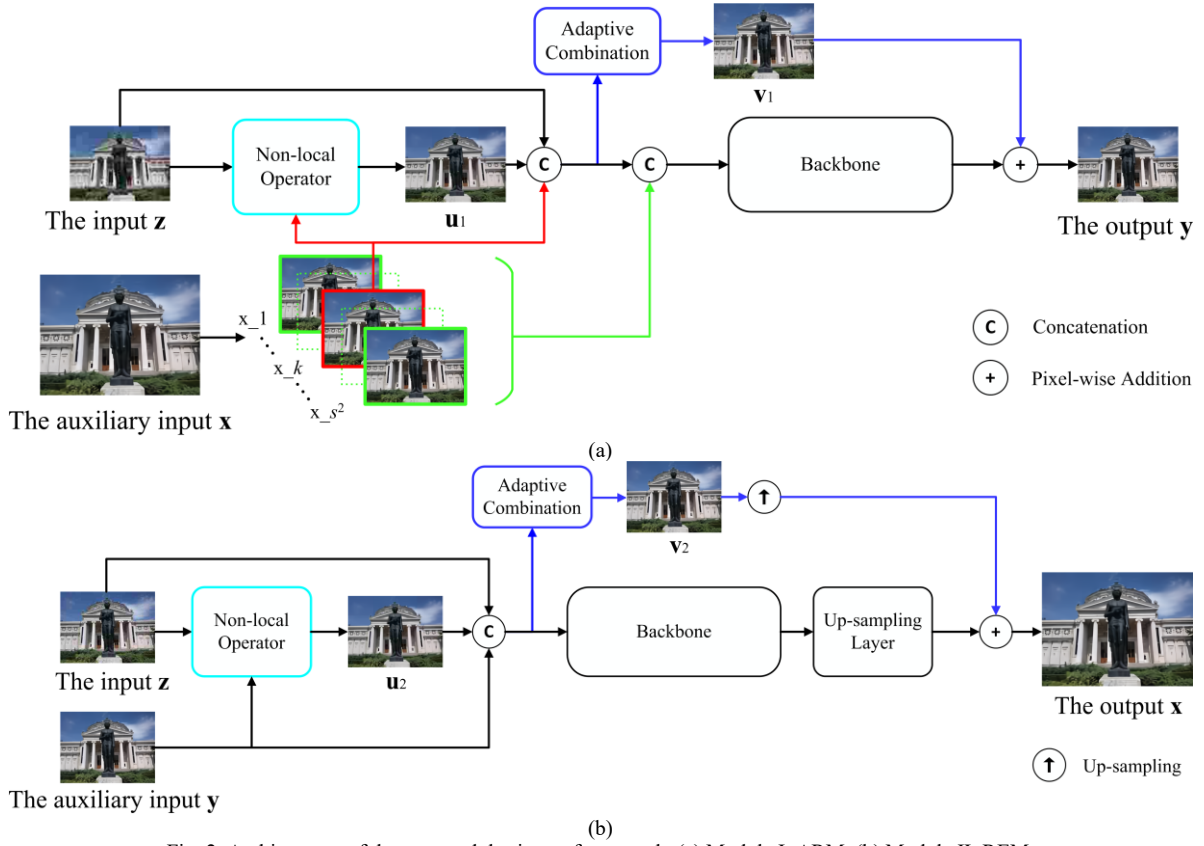


Fig. 2. Architectures of the two modules in our framework. (a) Module I: ARM. (b) Module II: REM.

concatenated images is exploited to fuse the pass-by information from different sources for the long skip connection.

It is worthwhile to note that the architectures of ARM and REM are not exactly the same. The reason is that the resolutions of the auxiliary inputs and the outputs are different for the two modules. In Module II, the resolution of the auxiliary input y is the same as that of the input z . Whereas, in Module I, the width and height of the auxiliary input x are s times larger than those of z , where s is the upscale factor. A straightforward idea is to down-scale x to the same resolution of z , just like the strategy in [23]. However, many important image details would be lost from x after down-scaling it. Hence, to keep the full information of x , we rearrange it into s^2 copies by using the space-to-depth transformation in [75], which can be regarded as the inverse process of pixel shuffle. All the copies, denoted as x_1, x_2, \dots, x_{s^2} , have similar image contents and have the same resolution as the input z . Among those copies, there exist sub-pixel displacements whose values are the multiples of $1/s$. According to the space-to-depth operator, the copy x_k is well registered with z , where k equals to the number rounding off $(s+1)/2$. Thus, this copy, highlighted in red in Fig. 2(a), is fed to the non-local operator and the adaptive combination for long skip connection. The remaining copies, marked in green in Fig. 2(a), are also concatenated with the pass-by information and then inputted into the backbone. Another difference between ARM and REM lies in the output end. In ARM, the output is of the same resolution with the input z , while the output resolution in REM is s^2 times larger than the input resolution. Thus, after the backbone in REM we deploy an up-sampling layer, which

consists of s^2 convolutional filters followed by an operation of pixel shuffle. Correspondingly, a simple up-sampling operator, such as bi-cubic interpolation, is adopted in the long skip connection.

In the followings, we will provide the details in the non-local operator and the adaptive combination, respectively.

1) Non-local operator

The idea of non-local means is to utilize the self-similarity of images [26], [27]. Similar patches or features from long-range positions are selected as candidates to recover local signals which may be lost due to artifacts or down-sampling. The non-local operator performed on the input z can be defined as

$$u_a(m) = \sum_n w(m, n) \cdot z(n), \quad (9)$$

where u_a is the output of non-local operator, a is 1 for Module I and 2 for Module II, m is the index of local patch to be recovered, n is the index of candidate patches over the whole image, and w is the similarity matrix of z . In (9), all the candidates are directly from the input z to prevent any processing or manipulation on the original signals.

For non-local operators, the measure of similarity is significant. When measuring the similarity in compressed images, we should be aware of the high similarity among the patches that are occupied by blocking artifacts. The horizontal or vertical signal patterns of blocking patches are highly similar to each other and may repeatedly appear in compressed images. Given a blocking patch, we wish to employ the patches that are similar

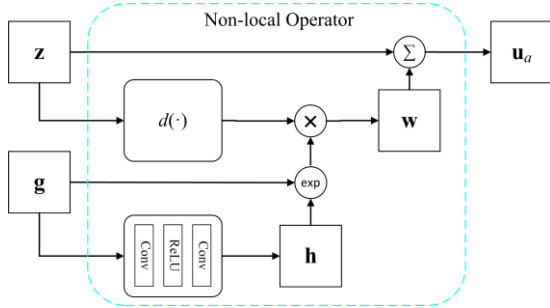


Fig. 3. Flowchart of our non-local operator.

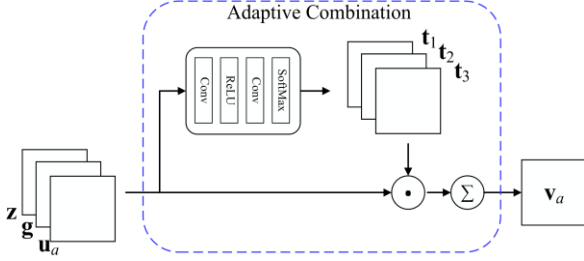


Fig. 4. Flowchart of our adaptive combination for long skip connection

to its image content, instead of its blocking pattern. Therefore, we resort to the auxiliary input to measure the similarity matrix \mathbf{w} . Specifically, the similarity between the m -th patch and the n -th one is calculated as

$$\mathbf{w}(m, n) = \frac{1}{N} \cdot \exp \left(-\frac{\|\mathbf{g}(m) - \mathbf{g}(n)\|^2}{\mathbf{h}(m)^2} \right) \cdot d(\mathbf{z}(n)), \quad (10)$$

where N is the normalized parameter to make the summation of each row in \mathbf{w} equals to 1, \mathbf{h} is an adaptive parameter map which will be explained later, and \mathbf{g} denotes an image from the auxiliary input. In Module I, \mathbf{g} is selected as the copy \mathbf{x}_k , and it is the auxiliary input itself in Module II. Thus, \mathbf{g} has exactly the same size with the input \mathbf{z} in both modules. In (10), we further include a binary function $d(\cdot)$ to detect the blocking edges in \mathbf{z} . This function returns 0 for blocking patches and 1 for others. In this work, we adopt the previous work in [76] to implement the detection function $d(\cdot)$. Both \mathbf{g} and $d(\cdot)$ are essential to calculate the similarity matrix \mathbf{w} . By using \mathbf{g} instead of \mathbf{z} to measure the patch distinction, we can pay attention to the candidate patches with similar contents rather than annoying blocking patterns. By using the binary function $d(\cdot)$, we can discard the blocking patches of \mathbf{z} in the calculation of (9). It means that some candidates with similar contents may still be excluded if they are severely contaminated by blocking artifacts in \mathbf{z} .

In the measure of the similarity matrix, the role of parameters \mathbf{h} is to control the sparsity degree of similarity matrix. Generally, a large value of the parameter would result in a smooth result, while a small one would produce artifacts and noises in \mathbf{u}_a . It has been demonstrated that the selection of \mathbf{h} has great impact on the results of non-local operator [71]. Moreover, its selection should depend on image content. For smooth regions, a large value of $\mathbf{h}(m)$ is preferred. For textural regions, the reverse applies. Therefore, in this work, we employ a simple convolutional neural network to adaptively estimate \mathbf{h} from \mathbf{g} .

This network only consists of two convolutional layers with a layer of rectified linear unit (ReLU) between them. Since the parameter map \mathbf{h} has the same size as \mathbf{g} , we get a pixel-wise control for the sparsity degree of similarity matrix.

The flowchart of our non-local operator is illustrated in Fig. 3. The non-local operators in ARM and REM utilize the same formulation and flowchart, but their learnable parameters are not shared during the training.

2) Adaptive combination for long skip connection

In the architectures of ARM and REM, we include a long skip connection, although there may already exist multiple short or long skip connections in the backbone. Instead of delivering learned features, the purpose of this skip connection is to pass the signals from the input end to the output end. Such an input-to-output pass-by has been demonstrated to be effective and necessary in solving the SISR problem [28]. In our architecture, after the non-local operator, three images, i.e., \mathbf{z} , \mathbf{g} , and \mathbf{u}_a , are available for the long skip connection. Their properties are different. The input \mathbf{z} is the signal remained unprocessed, but it may suffer from severe artifacts. The image \mathbf{g} is from the auxiliary input, which is assumed to be a clean signal. However, since the auxiliary input of one module is the output of the other one, some fake signal patterns would be introduced into \mathbf{g} when we train the other module by external samples. The image \mathbf{u}_a is from the non-local operator and much cleaner than the input \mathbf{z} . Although \mathbf{u}_a is also a processed image, all the signal patterns in \mathbf{u}_a are from the input \mathbf{z} itself. Therefore, it is not wise to ignore any one of the three images for the long skip connection. In this work, we use a convex combination with adaptive weights to fuse them to one image. That is

$$\mathbf{v}_a = \mathbf{t}_1 \odot \mathbf{z} + \mathbf{t}_2 \odot \mathbf{g} + \mathbf{t}_3 \odot \mathbf{u}_a \quad (11)$$

subject to $\mathbf{t}_1 + \mathbf{t}_2 + \mathbf{t}_3 = \mathbf{1}$,

where \mathbf{v}_a is the output of adaptive combination, the subscript a indicates Module I or Module II, \mathbf{t}_1 , \mathbf{t}_2 , and \mathbf{t}_3 are the weight maps for \mathbf{z} , \mathbf{g} , and \mathbf{u}_a respectively, \odot represents the pixel-wise multiplication, and $\mathbf{1}$ denotes the map of all ones. As demonstrated in [77], the identity mapping is the best option for residual learning. Thus, the constraint on the summation of \mathbf{t}_1 , \mathbf{t}_2 , and \mathbf{t}_3 is essential to make our long skip connection approximate the identity mapping. Obviously, the weight maps in (11) depend on the image contents and qualities of \mathbf{z} , \mathbf{g} , and \mathbf{u}_a . Thus, similar to the adaptive parameter \mathbf{h} in (10), we employ a light network to estimate \mathbf{t}_1 , \mathbf{t}_2 , and \mathbf{t}_3 from \mathbf{z} , \mathbf{g} , and \mathbf{u}_a . This network consists of two convolutional layers, which are followed by a ReLU layer and a SoftMax operation, respectively. The SoftMax operation is performed on each pixel position to satisfy the constraint in (11). The flowchart of our adaptive combination is summarized in Fig. 4.

C. Training and Loss Function

As described in Section III.A, each module of the proposed model has two inputs: the first is the compressed LR image \mathbf{z} , and the second is the output from the other module. Hence, our model is a recurrent system naturally, which can be unfolded in

time to facilitate its training [25], [43]. Supposing the maximum unfolding time step is J , we can rewrite (7) and (8) to

$$\begin{aligned} \mathbf{y}_j &= \mathcal{P}(\mathbf{x}_{j-1}, \mathbf{z}; \Theta_1) \\ \mathbf{x}_j &= \mathcal{R}(\mathbf{y}_j, \mathbf{z}; \Theta_2), \end{aligned}$$

where $j \leq J$ indicates the index of time step. When j equals to 1, the auxiliary input for Module I, i.e., \mathbf{x}_0 , is not available. For simplicity, we bicubically interpolate the compressed input \mathbf{z} to obtain the initial estimation \mathbf{x}_0 . The learnable parameters Θ_1 and Θ_2 are shared across time steps.

At each time step j , we have two results, implying two terms are required in the loss during the model training. Furthermore, following the suggestion in [43], we tie the loss for every time step. Therefore, the loss function L is given by

$$L(\Theta_1, \Theta_2) = \sum_{j=1}^J \rho_j \left(\|\mathcal{P}(\mathbf{x}, \mathbf{z}; \Theta_1) - \mathbf{y}\| + \gamma \|\mathcal{R}(\mathbf{y}, \mathbf{z}; \Theta_2) - \mathbf{x}\| \right) \quad (12)$$

where ρ_j controls loss weight of each time step, and γ balances the impacts of ARM and REM. During the unfolding, it is tolerable that the model has relatively poor performance at first few time steps. According to curriculum learning strategy [78], we regard the training in first few time steps as easy tasks by setting smaller loss weights ρ_j for smaller j . Using the unfolding technique and the loss defined in (12), an end-to-end training is performed to fix the parameters Θ_1 and Θ_2 in our model. After training the model, for a given LR compressed image, the proposed model can produce J results for \mathbf{x} . And the J -th one is selected as our final result.

IV. EXPERIMENTS

In this section, we will provide implementation details and the dataset used in our experiments at first. Subsequently, we compare the proposed method with state-of-the-art SR methods. Then, ablation studies are conducted to demonstrate the effectiveness of different parts in the proposed method. Finally, a real-world testing is presented to show the generalization ability of our method.

A. Implementation Details and Dataset

The proposed method is implemented in PyTorch on a machine of NVIDIA GeForce 1080Ti. Two versions of our model are included in the following comparisons. One is named as tiny model, and the other one is called full model. The number of learnable parameters in the backbone of tiny model is much smaller than that of full model. Specifically, we adopt 5 residual groups from RCAN as the backbone for each module in our full model. In our tiny model, only 2 residual groups are employed for each module. Moreover, each residual group in our tiny or full model contains 12 channel attention blocks, instead of 20 attention blocks used in the original RCAN model. Thus, our full model is still much lighter than RCAN. In addition to the convolutional layers in the backbone, there are two convolutional layers in the non-local operator, as shown in Fig. 3, and two convolutional layers in the adaptive combination, as

shown in Fig. 4. Among these four layers, the kernel size of the first convolutional layer in Fig. 3 is 3×3 , while the kernel sizes of the rest are 1×1 . The numbers of their output channel are 64, 1, 64, and 3, respectively. The maximum unfolding time step J is empirically set to 3 for our full model and 5 for our tiny one. Correspondingly, we set ρ_j in (12) as $\{0.3, 0.6, 1\}$ for the full model and $\{0.2, 0.4, 0.6, 0.8, 1\}$ for the tiny one. The parameter γ in the loss function is simply set to 1.

Two widely-used compression types, known as JPEG [73] and WebP [80], are involved in our experiments. For each type of compression, we further involve 5 compression levels or quality factors (QFs). Specifically, for the JPEG compression, we have QFs of 10, 20, 30, 40, and 50. For the WebP compression, QFs of 5, 10, 20, 30, and 40 are utilized. Hence, to compress an LR image, we have totally 10 kinds of compression configurations, viz., 2 compression types multiplied by 5 QFs. Furthermore, three scaling factors ($2\times$, $3\times$, and $4\times$) are involved in this work. For each up-scaling factor, we train a tiny model and a full model over all the compression configurations. In other words, LR images with various compression configurations are mixed together to train and test our models. Since our focus is on the compression of LR images rather than down-sampling kernels, the bicubic down-sampling is employed to resize images for simplicity. To prepare training and validation data, compressed LR images are generated by first down-sampling and then compressing the samples in DIV2K [81]. Data augmentation is also performed on the training pairs by random rotation and flipping. In each training batch, we randomly crop 32 patches with the size of 48×48 as LR inputs. Our models are trained by the ADAM optimizer [79] with an initial learning rate of 10^{-4} . The training is stopped if the model performance on the validation set decreases.

In addition to training and validation data, we also require to prepare a testing dataset with ground truths to facilitate quantitative comparisons. Ground truths should be uncompressed HR images. However, most publicly available image databases suffer from compression to some extent. As an exception, the Kodak dataset [82] contains 24 lossless images, which are used to produce our testing dataset. Moreover, we capture another 76 uncompressed images in various scenarios by ourselves. For more details about these captured images, one can refer to our online supplementary materials in [83]. Totally, 100 lossless HR images can be used as ground truths in our quantitative tests. By using these 100 images and the abovementioned compression configurations, we produce 1000 testing LR images for each up-scaling factor.

B. Comparisons

To show the effectiveness of the proposed method, we compare it with some state-of-the-art SISR models, including ICSD [23], CISRDCNN [24], SAN [39], RCAN [38], and USRNet [57]. Among these competitors, ICSD is a traditional method, while all the others are based on deep networks. The models of ICSD and CISRDCNN are specifically designed for CISR. The models of SAN and RCAN are presented only for clean LR images. The USRNet model is applicable to either clean images or noisy and blurred images. For fair comparisons, we add a pre-processing before SAN, RCAN, and USRNet to reduce

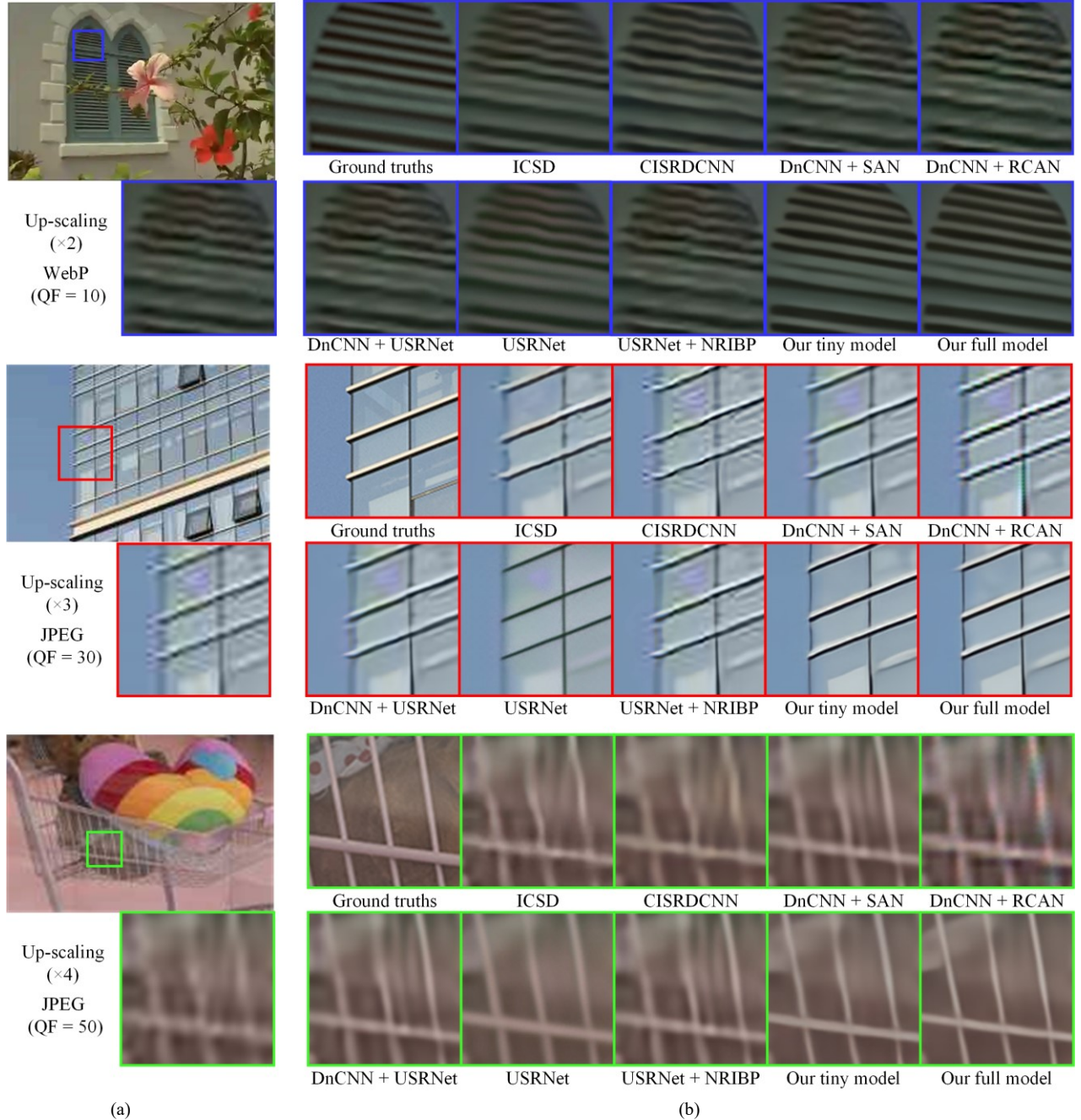


Fig. 5. Visual comparisons. (a) Several compressed LR images for testing. (b) Ground truths and results of different SISR methods.

compression artifacts. Here, the pre-processing is achieved by DnCNN [65], which is a widely-used model trained to reduce compression artifacts for a large range of QFs. The USRNet model can further incorporate noise levels and blur kernels of LR images. It would be interesting to see whether the SISR performance is satisfying when compression artifacts are treated as noises and blurring. Thus, we also provide the SR results that are obtained by applying USRNet alone. To estimate noise levels and blur kernels for USRNet, we adopt the methods in [84] and [85], respectively. Moreover, the method of NRIBP [51] can be combined with SR models to suppress the noises and artifacts in SR results, e.g., USRNet + NRIBP. The codes of ICSD, CISRDCNN, and NRIBP are implemented by ourselves, while the rest codes are provided by their authors. Here, we provide visual and quantitative comparisons in Fig. 5

and Table I. One can refer to our online materials in [83] for more results in comparison with more SISR methods, including A+ [12] and EDSR [34].

In Fig. 5(a), we show three examples of testing LR images, which are heavily compressed by JPEG or WebP. In each image, we highlight an image region, whose results from different SISR models are exhibited in Fig. 5(b). From the results of highlighted regions in Fig. 5(b), we can find that results from some competitors suffer from conspicuous artifacts. At the same time, the results from other compared SISR models are over-smoothed. In contrast, our models can successfully retrieve sharp edges as well as remove artifacts. Moreover, the results from our tiny model are visually comparable with those from our full model, although the former one is much lighter than the latter one.

Four criteria are used to quantitatively measure the performance of different SR methods. They are peak signal to noise ratio (PSNR), structural similarity (SSIM) index [86], information fidelity criterion (IFC) [87], and structure-texture decomposition for image quality assessment of SRIs (SIS) [88]. PSNR and SSIM are widely adopted in the evaluation of SRIs. And it has been demonstrated in [1] and [88] that IFC and SIS have relatively high correlations with the perceptual quality of SRIs. Therefore, it is appropriate to include these four criteria in quantitative comparisons. For all these criteria, larger values imply better performance. Quantitative results of competitors and our models are provided in Table I, which contains three up-scaling factors. For each up-scaling factor in Table I, the listed values are the average results over 1000 testing images. In Table I, the best performance is highlighted in bold, and the second-best results are distinguished by italics. From Table I, we can see that our full model achieves an improvement of 0.5–0.6 dB on PSNR. On the other three criteria, its superiority to the competitors is also remarkable. Even our tiny model can achieve impressive performance on all the criteria, although it is much lighter than our full model.

To show the performance of the proposed models across different compression configurations, we list detailed results based on PSNR in Table II. There are 100 testing images for each compression configuration. Thus, each PSNR value in Table II are the average result over 100 images. Table II shows the superiority of our models, although they are trained on a mixed set of various compressed images. Detailed results based on SSIM, IFC, and SIS can be found in [83]. In conclusion, the visual and quantitative comparisons in Fig. 5 and Tables I–II demonstrate the effectiveness of our models.

In addition to SISR results, we would like to compare our results of compression artifacts reduction, i.e., the output of Module I, with several classical and state-of-the-art methods, including SA-DCT [61], TNRD [69], DnCNN [65], and DCSC [67]. Quantitative and visual comparisons for the compression artifacts reduction can be accessed in our online materials [83].

C. Ablation Studies

In this sub-section, we would like to conduct ablation studies to show the effectiveness of different parts in our model. For simplicity, only our tiny model is investigated here, and only PSNR values are recorded. Moreover, ablation studies are only performed on the case that LR images compressed by JPEG with QF = 10 are super-resolved by a factor of 2.

Parallel and series data streams are essential in the proposed framework. The compressed LR input is simultaneously received and processed by Module I and Module II in parallel. Meanwhile, two cascaded streams are realized by introducing the output of one module to the input of other one. That is, each module has two inputs. Thus, we can investigate the importance of different streams by shutting down one of these inputs. Here, for convenience, we denote two inputs of Module I as I-CI and I-AI: I-CI is the compressed image received by Module I, and I-AI is the auxiliary input for Module I. In the same abbreviation manner, two inputs of Module II are defined as II-CI and II-AI. The results based on PSNR in the first row of Table III indicates that the performance declines if we cut off any stream from I-CI, I-AI, II-CI, and II-AI. Therefore, we can conclude that all the streams in our method are indispensable.

TABLE I
QUANTITATIVE COMPARISONS BASED ON PSNR, SSIM, IFC, AND SIS

Up-scaling factor	SR Models	Criteria			
		PSNR	SSIM	IFC	SIS
2	ICSD	28.86	0.7903	1.7968	0.6662
	CISRDCNN	29.31	0.8019	1.8964	0.7094
	DnCNN + SAN	29.48	0.8027	1.8815	0.7223
	DnCNN + RCAN	28.67	0.7927	1.7316	<i>0.7540</i>
	DnCNN + USRNet	29.49	0.8028	1.8850	0.7212
	USRNet	28.59	0.7682	1.6711	0.6381
	USRNet + NRIBP	29.47	0.8020	1.8619	0.7216
	Our tiny model	29.97	<i>0.8149</i>	<i>2.0978</i>	<i>0.7495</i>
	Our full model	30.10	0.8181	2.1521	0.7576
3	ICSD	26.82	0.7259	1.1362	0.4956
	CISRDCNN	27.37	0.7391	1.2406	0.5287
	DnCNN + SAN	27.40	0.7384	1.2151	0.5374
	DnCNN + RCAN	26.75	0.7245	1.0905	0.5845
	DnCNN + USRNet	27.43	0.7392	1.2208	0.5399
	USRNet	26.86	0.7159	1.1387	0.4637
	USRNet + NRIBP	27.40	0.7378	1.2022	0.5397
	Our tiny model	<i>27.84</i>	<i>0.7536</i>	<i>1.3947</i>	<i>0.5864</i>
	Our full model	27.94	0.7564	1.4355	0.5893
4	ICSD	25.54	0.6820	0.7974	0.3702
	CISRDCNN	25.99	0.6959	0.8995	0.3691
	DnCNN + SAN	26.16	0.6954	0.8767	0.3843
	DnCNN + RCAN	25.65	0.6808	0.7799	0.4167
	DnCNN + USRNet	26.18	0.6964	0.8811	0.3863
	USRNet	25.65	0.6759	0.8175	0.3251
	USRNet + NRIBP	26.16	0.6950	0.8670	0.3883
	Our tiny model	<i>26.55</i>	<i>0.7117</i>	<i>1.0267</i>	<i>0.4404</i>
	Our full model	26.62	0.7138	1.0504	0.4418

Moreover, we investigate the impact of our non-local operator by removing it and replacing it with a traditional non-local operator. For the traditional non-local operator, we empirically set all the elements in \mathbf{h} to 30. Similarly, we can investigate the effect of our adaptive combination for skip connection by using only one of \mathbf{z} , \mathbf{g} , and \mathbf{u}_s for the global residual learning. Besides, the result from the model without such a long skip connection is also recorded. All these results are provided in the second and third rows of Table III, which demonstrate our non-local operator and adaptive combination are beneficial.

D. Super-resolving Real-World Compressed Images

We further investigate the practicability of our method by testing some images downloaded from the Internet. Two examples are illustrated in Fig. 6, which are the SR results of our full model. More visual examples can be found in our online materials [83]. It can be observed that our model can well reduce compression artifacts as well as recover image details.

V. CONCLUSION

In this paper, we propose a parallel and cascaded framework to super-resolve compressed LR images. This framework includes two modules: ARM and REM. Both modules are based on deep neural networks and share similar network architectures. Between ARM and REM, both parallel and series flows are included. On one hand, compressed LR images is received and processed by ARM and REM in a parallel way. As a consequence, the original information in input images is fully available for both modules without any loss or change. On the other hand, two series flows are formed by regarding the output of one module as the auxiliary input of the other one. These

TABLE II
QUANTITATIVE COMPARISONS FOR DIFFERENT COMPRESSION CONFIGURATIONS BASED ON PSNR

Up-scaling factor	SR Models	Compression Configurations (Compression type & QF)									
		JPEG & 10	JPEG & 20	JPEG & 30	JPEG & 40	JPEG & 50	WebP & 5	WebP & 10	WebP & 20	WebP & 30	WebP & 40
2	ICSD	26.96	28.31	29.02	29.52	29.90	29.38	27.60	28.09	28.69	29.05
	CISRDCNN	27.51	28.91	29.62	30.07	30.41	27.88	28.57	29.45	30.07	30.54
	DnCNN + SAN	27.68	29.14	29.91	30.41	30.82	27.72	28.46	29.48	30.27	30.92
	DnCNN + RCAN	27.35	28.49	29.04	29.38	29.63	27.36	27.93	28.67	29.21	29.64
	DnCNN + USRNet	27.68	29.12	29.90	30.42	30.82	27.74	28.48	29.51	30.28	30.93
	USRNet	27.23	28.41	28.93	29.20	29.38	27.60	28.09	28.69	29.05	29.28
	USRNet + NRIBP	27.57	29.05	29.87	30.40	30.81	27.73	28.47	29.52	30.30	30.96
	Our tiny model	28.01	29.51	30.31	30.84	31.25	28.41	29.11	30.07	30.81	31.41
	Our full model	28.11	29.61	30.43	30.95	31.37	28.56	29.26	30.20	30.93	31.53
3	ICSD	25.35	26.41	26.94	27.31	27.58	25.82	26.41	27.02	27.49	27.88
	CISRDCNN	25.90	27.05	27.62	27.98	28.22	26.27	26.84	27.53	28.00	28.36
	DnCNN + SAN	25.97	27.09	27.67	28.06	28.34	26.09	26.69	27.49	28.08	28.55
	DnCNN + RCAN	25.70	26.59	27.02	27.26	27.45	25.74	26.20	26.78	27.19	27.51
	DnCNN + USRNet	25.96	27.09	27.68	28.08	28.37	26.09	26.72	27.53	28.13	28.61
	USRNet	25.59	26.63	27.09	27.35	27.52	26.03	26.48	27.02	27.33	27.55
	USRNet + NRIBP	25.87	27.03	27.65	28.05	28.36	26.08	26.70	27.53	28.13	28.62
	Our tiny model	26.22	27.43	28.08	28.49	28.78	26.65	27.23	27.98	28.54	28.99
	Our full model	26.31	27.53	28.18	28.59	28.88	26.78	27.35	28.09	28.63	29.07
4	ICSD	24.29	25.20	25.65	25.97	26.19	24.75	25.12	25.73	26.11	26.45
	CISRDCNN	24.73	25.70	26.17	26.46	26.66	25.09	25.56	26.14	26.53	26.81
	DnCNN + SAN	24.88	25.87	26.37	26.70	26.94	25.04	25.56	26.27	26.78	27.17
	DnCNN + RCAN	24.68	25.50	25.87	26.10	26.27	24.75	25.17	25.71	26.06	26.34
	DnCNN + USRNet	24.87	25.87	26.39	26.72	26.97	25.05	25.59	26.31	26.83	27.23
	USRNet	24.48	25.40	25.81	26.05	26.21	24.95	25.35	25.82	26.09	26.28
	USRNet + NRIBP	24.81	25.83	26.36	26.70	26.96	25.04	25.58	26.30	26.83	27.23
	Our tiny model	25.12	26.21	26.76	27.11	27.36	25.53	26.03	26.71	27.19	27.56
	Our full model	25.17	26.25	26.81	27.17	27.44	25.62	26.13	26.78	27.25	27.62

TABLE III
ABLATION STUDIES BASED ON PSNR

w/o [†] I-CI	w/o I-AI	w/o II-CI	w/o II-AI	Ours
27.93	27.91	27.93	27.88	
w/o non-local operator		Traditional non-local operator		
27.94		27.95		
w/o residual	z as residual	g as residual	u_a as residual	
27.90	27.95	27.96	27.97	

[†]“w/o” means without

series streams enable the information exchange between ARM and REM so that the two modules can facilitate each other. Furthermore, to make better use of the auxiliary inputs, our non-local operator and adaptive combination are presented with learnable parameters in each module. Experiments are conducted on the LR images with various compression configurations. Extensive comparisons demonstrate the advantage of the proposed model over state-of-the-art SISR models. And the advantage is more significant for heavily compressed images. Ablation studies are finally performed to show the contribution of different parts in our model.

REFERENCES

- [1] C.-Y. Yang, C. Ma, and M.-H. Yang, “Single-image super-resolution: A benchmark,” in *Proc. Eur. Conf. Comput. Vis.*, 2014, pp. 372–386.
- [2] Y. Hu, K. Lam, G. Qiu, and T. Shen, “From local pixel structure to global image super-resolution: A new face hallucination framework,” *IEEE Trans. Image Process.*, vol. 20, no. 2, pp. 433–445, Feb. 2011.
- [3] W. W. W. Zou and P. C. Yuen, “Very low resolution face recognition problem,” *IEEE Trans. Image Process.*, vol. 21, no. 1, pp. 327–340, 2012.
- [4] Z. Xiong, X. Sun, and F. Wu, “Super-resolution for low quality thumbnail images,” in *Proc. IEEE Int. Conf. Multimedia & Expo*, pp. 181–184, 2008.
- [5] X. Li and M. T. Orchard, “New edge-directed interpolation,” *IEEE Trans. Image Process.*, vol. 10, no. 10, pp. 1521–1527, Oct. 2001.
- [6] G. Qiu, “Interresolution look-up table for improved spatial magnification of image,” *J. Vis. Commun. Image Represent.*, vol. 11, no. 4, pp. 360–373, Dec. 2000.
- [7] Q. Wang and R. K. Ward, “A new orientation-adaptive interpolation method,” *IEEE Trans. Image Process.*, vol. 16, no. 4, pp. 889–900, 2007.
- [8] K. I. Kim and Y. Kwon, “Single-image super-resolution using sparse regression and natural image prior,” *IEEE Trans. Pattern Anal. Mach. Intell.*, vol. 32, no. 6, pp. 1127–1133, Jun. 2010.

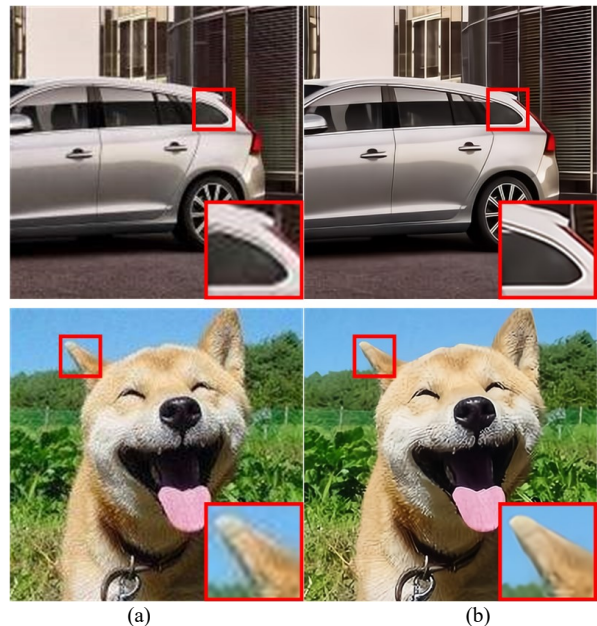


Fig. 6. Testing on real-world compressed images. (a) Bicubically interpolated LR images with scale factor 2. (b) Our results with scale factor 2.

- [9] J. Yang, J. Wright, T. S. Huang, and Y. Ma, "Image super-resolution via sparse representation," *IEEE Trans. Image Process.*, vol. 19, no. 11, pp. 2861–2873, Nov. 2010.
- [10] W. Dong, L. Zhang, G. Shi, and X. Wu, "Image deblurring and super-resolution by adaptive sparse domain selection and adaptive regularization," *IEEE Trans. Image Process.*, vol. 20, pp. 1838–1857, 2011.
- [11] K. S. Ni, and T. Q. Nguyen, "Image super resolution using support vector regression," *IEEE Trans. Image Process.*, vol. 16, pp.1596–1610, 2007.
- [12] R. Timofte, V. De, and L. Van Gool, "A+: Adjusted anchored neighborhood regression for fast super-resolution," in *Proc. IEEE Asian Conf. Comput. Vis.*, 2014, pp. 111–126.
- [13] H. Wang, X. Gao, K. Zhang, and J. Li, "Single-image super-resolution using active-sampling Gaussian process regression," *IEEE Trans. Image Process.*, vol. 25, no. 2, pp. 935–948, Feb. 2016.
- [14] C. Dong, C. C. Loy, K. He, and X. Tang, "Image super-resolution using deep convolutional networks," *IEEE Trans. Pattern Anal. Mach. Intell.*, vol. 38, no. 2, pp. 295–307, Feb. 2016.
- [15] W. Yang, X. Zhang, Y. Tian, W. Wang, J.-H. Xue, and Q. Liao, "Deep learning for single image super-resolution: A brief review," *IEEE Trans. Multimedia*, vol. 21, no. 12, pp. 3106–3121, Dec. 2019.
- [16] Z. Wang, J. Chen, S. C.H. Hoi, "Deep learning for image super resolution: A survey," *IEEE Trans. Pattern Anal. Mach. Intell.*, Early Access, pp. 1–22, DOI: 10.1109/TPAMI.2020.2982166.
- [17] T. Kohler, M. Batz, F. Naderi, A. Kaup, A. Maier, and C. Riess, "Toward bridging the simulated-to-real gap: benchmarking super-resolution on real data," *IEEE Trans. Pattern Anal. Mach. Intell.*, vol. 42, no. 11, pp. 2944–2959, Nov. 2020.
- [18] A. Singh, F. Porikli and N. Ahuja, "Super-resolving noisy images," in *Proc. IEEE Conf. Comput. Vis. Pattern Recognit.*, 2014, pp. 2846–2853.
- [19] J. Cai, H. Zeng, H. Yong, Z. Cao, and L. Zhang, "Toward real-world single image super-resolution: A new benchmark and a new model," in *Proc. Int. Conf. Comput. Vis.*, 2019, pp. 3086–3095.
- [20] Z. Xiong, X. Sun, and F. Wu, "Robust web image/video super resolution," *IEEE Trans. Image Process.*, vol. 19, no. 8, pp. 2017–2028, 2010.
- [21] L.-W. Kang, C.-C. Hsu, B. Zhuang, C.-W. Lin, and C.-H. Yeh, "Learning-based joint super-resolution and deblocking for a highly compressed image," *IEEE Trans. Multimedia*, vol. 17, no. 7, pp. 921–934, Jul. 2015.
- [22] O.-Y. Lee, J.-W. Lee, D.-Y. Lee, and J.-O. Kim, "Joint super-resolution and compression artifact reduction based on dual-learning," in *Proc. Int. Conf. Vis. Commun. Image Process.*, 2016, pp. 1–4.
- [23] T. Li, X. He, L. Qing, Q. Teng, and H. Chen, "An iterative framework of cascaded deblocking and superresolution for compressed images," *IEEE Trans. Multimedia*, vol. 20, no. 6, pp. 1305–1320, Jun. 2018.
- [24] H. Chen, X. He, C. Ren, L. Qing, and Q. Teng, "CISRDCNN: Super-resolution of compressed images using deep convolutional neural networks," *Neurocomputing*, vol. 285, pp. 204–219, 2018.
- [25] A. R. Zamir, T.-L. Wu, L. Sun, W. B. Shen, and B. E. Shi, "Feedback networks," in *Proc. IEEE Conf. Comput. Vis. Pattern Recognit.*, 2017, pp. 1308–1317.
- [26] A. Buades, B. Coll, and J.-M. Morel, "Nonlocal image and movie denoising," *Int. J. Comput. Vis.*, vol. 76, no. 2, pp. 123–139, 2007.
- [27] X. Wang, R. Girshick, A. Gupta, and K. He, "Non-local networks," in *Proc. IEEE Conf. Comput. Vis. Pattern Recognit.*, 2018, pp. 7794–7803.
- [28] J. Kim, J. K. Lee, and K. M. Lee, "Accurate image super-resolution using very deep convolutional networks," in *Proc. IEEE Conf. Comput. Vis. Pattern Recognit.*, Jun. 2016, pp. 1646–1654.
- [29] K. He, X. Zhang S. Ren, and J. Sun, "Deep residual learning for image recognition," in *Proc. IEEE Conf. Comput. Vis. Pattern Recognit.*, Jun. 2016, pp. 770–778.
- [30] W. T. Freeman, T. R. Jones, and E. C. Pasztor, "Example-based super-resolution," *IEEE Comput. Graph. Appl.*, vol. 22, no. 2, pp. 56–65, 2002.
- [31] X. Li, K. M. Lam, G. Qiu, L. Shen, and S. Wang, "Example-based super-resolution with class-specific predictors," *J. Vis. Commun. Image Represent.*, vol. 20, no. 5, pp. 321–322, Jul. 2009.
- [32] H. Chang, D.-Y. Yeung, and Y. Xiong, "Super-resolution through neighbor embedding," in *Proc. IEEE Conf. Comput. Vis. Pattern Recognit.*, Jun. 2004, pp. 1-275–1-282.
- [33] D. Liu, Z. Wang, B. Wen, J. Yang, W. Han, and T. S. Huang, "Robust single image super-resolution via deep networks with sparse prior," *IEEE Trans. Image Process.*, vol. 25, no. 7, pp. 3194–3207, Jul. 2016.
- [34] B. Lim, S. Son, H. Kim, S. Nah, and K. M. Lee, "Enhanced deep residual networks for single image super-resolution," in *Proc. IEEE Conf. Comput. Vis. Pattern Recognit. Workshops*, 2017, pp. 1132–1140.
- [35] Y. Tai, J. Yang, X. Liu, and C. Xu, "MemNet: A persistent memory network for image restoration," in *Proc. IEEE Int. Conf. Comput. Vis.*, 2017, pp. 4549–4557.
- [36] Y. Zhang, Y. Tian, Y. Kong, B. Zhong, and Y. Fu, "Residual dense network for image super-resolution," in *Proc. IEEE Conf. Comput. Vis. Pattern Recognit.*, 2018, pp. 2472–2481.
- [37] M. Haris, G. Shakhnarovich, and N. Ukita, "Deep back-projection networks for super-resolution," in *Proc. IEEE Conf. Comput. Vis. Pattern Recognit.*, 2018, pp. 1664–1673.
- [38] Y. Zhang, K. Li, K. Li, L. Wang, B. Zhong, and Y. Fu, "Image super-resolution using very deep residual channel attention networks," in *Proc. Eur. Conf. Comput. Vis.*, 2018, pp. 294–310.
- [39] T. Dai, J. Cai, Y. Zhang, S.-T. Xia, and L. Zhang, "Second-order attention network for single image super-resolution," in *Proc. IEEE Conf. Comput. Vis. Pattern Recognit.*, 2019, pp. 11057–11066.
- [40] J. Kim, J. K. Lee, and K. M. Lee, "Deeply-recursive convolutional network for image super-resolution," in *Proc. IEEE Conf. Comput. Vis. Pattern Recognit.*, 2016, pp. 1637–1645.
- [41] Y. Tai, J. Yang, and X. Liu, "Image super-resolution via deep recursive residual network," in *Proc. IEEE Conf. Comput. Vis. Pattern Recognit.*, 2017, pp. 2790–2798.
- [42] W. Han, S. Chang, D. Liu, M. Yu, M. Witbrock, and T. S. Huang, "Image super-resolution via dual-state recurrent networks," in *Proc. IEEE Conf. Comput. Vis. Pattern Recognit.*, 2018, pp. 1654–1663.
- [43] Z. Li, J. Yang, Z. Liu, X. Yang, G. Jeon, W. Wu, "Feedback network for image super-resolution," in *Proc. IEEE Conf. Comput. Vis. Pattern Recognit.*, 2019, pp. 3862–3871.
- [44] W. Dong, L. Zhang, R. Lukac, and G. Shi, "Sparse representation based image interpolation with nonlocal autoregressive modeling," *IEEE Trans. Image Process.*, vol. 22, no. 4, pp.1382–1394, Apr. 2013.
- [45] C. Ren, X. He, Q. Teng, Y. Wu, T. Q. Nguyen, "Single image super-resolution using local geometric duality and non-local similarity," *IEEE Trans. Image Process.*, vol. 25, no. 5, pp. 2168–2183, May. 2016.
- [46] C. Ren, X. He, and T. Q. Nguyen, "Single image super-resolution via adaptive high-dimensional non-local total variation and adaptive geometric feature," *IEEE Trans. Image Process.*, vol. 26, pp. 90–106, 2017.
- [47] Z.-S. Liu, L.-W. Wang, C.-T. Li, W.-C. Siu, and Y.-L. Chan, "Image super-resolution via attention based back projection networks," in *Proc. Int. Conf. Comput. Vis., Workshops*, 2019, pp. 3517–3525.
- [48] T. Dai, H. Zha, Y. Jiang, and S.-T. Xia, "Image super-resolution via residual block attention networks," in *Proc. Int. Conf. Comput. Vis., Workshops*, 2019, pp. 3879–3886.
- [49] O.-Y. Lee, J.-W. Lee, and J.-O. Kim, "Combining self-learning based super-resolution with denoising for noisy images," *J. Vis. Commun. Image Represent.*, vol. 48, pp. 66–76, 2017.
- [50] S. Huang, *et al.*, "Robust single-image super-resolution based on adaptive edge-preserving smoothing regularization," *IEEE Trans. Image Process.*, vol. 27, no. 6, pp. 2650–2663, Jun. 2018.
- [51] J.-S. Yoo and J.-O. Kim, "Nose-robust iterative back-projection," *IEEE Trans. Image Process.*, vol. 29, pp. 1219–1232, 2020.
- [52] K. Zhang, W. Zuo, and L. Zhang, "Learning a single convolutional super-resolution network for multiple degradations," in *Proc. IEEE Conf. Comput. Vis. Pattern Recognit.*, 2018, pp. 3262–3271.
- [53] K. Zhang, W. Zuo, and L. Zhang, "Deep plug-and-play super-resolution for arbitrary blur kernels," in *Proc. IEEE Conf. Comput. Vis. Pattern Recognit.*, 2019, pp. 1671–1681.
- [54] C. Ledig *et al.*, "Photo-realistic single image super-resolution using a generative adversarial network," in *Proc. IEEE Conf. Comput. Vis. Pattern Recognit.*, Jul. 2017, pp. 105–114.
- [55] Y. Zhang, *et al.*, "Multiple cycle-in-cycle generative adversarial networks for unsupervised image super-resolution," *IEEE Trans. Image Process.*, vol. 29, pp. 1101–1112, 2020.
- [56] X. Hu, *et al.*, "Meta-USR: A unified super-resolution network for multiple degradation parameters," *IEEE Trans. Neural Netw. Learn. Syst.*, Early Access, pp. 1–15, DOI: 10.1109/TNNLS.2020.3016974.
- [57] K. Zhang, L. V. Gool, and R. Timofte, "Deep unfolding network for image super-resolution," in *Proc. IEEE Conf. Comput. Vis. Pattern*

- Recognit.*, 2020, pp. 3217–3226.
- [58] J. G. Apostolopoulos and N. S. Jayant, “Postprocessing for very low bit-rate video compression,” *IEEE Trans. Image Process.*, vol. 8, no. 8, pp. 1125–1129, Aug. 1999.
- [59] D. Sun and W.-K. Cham, “Postprocessing of low bit-rate block DCT coded images based on a fields of experts prior,” *IEEE Trans. Image Process.*, vol. 16, no. 11, pp. 2743–2751, Nov. 2007.
- [60] G. Triantafyllidis, D. Tzovaras, and M. G. Strintzis, “Blocking artifact detection and reduction in compressed data,” *IEEE Trans. Circuits Syst. Video Technol.*, vol. 12, no. 10, pp. 877–890, Oct. 2002.
- [61] A. Foi, V. Katkovnik, and K. Egiazarian, “Pointwise shape-adaptive DCT for high-quality denoising and deblocking of grayscale and color images,” *IEEE Trans. Image Process.*, vol. 16, no. 5, pp. 1395–1411, 2007.
- [62] C. Chang, Y. Deng, C. C. Loy, and X. Tang, “Compression artifacts reduction by a deep convolutional network,” in *Proc. IEEE Conf. Comput. Vis. Pattern Recognit.*, 2015, pp. 576–584.
- [63] J. Guo and H. Chao, “Building dual-domain representations for compression artifacts reduction,” in *Proc. Eur. Conf. Comput. Vis.*, 2016, pp. 628–644.
- [64] Z. Wang, D. Liu, S. Chang, Q. Ling, Y. Yang, and T. S. Huang, “D³: Deep dual-domain based fast restoration of JPFPG-compressed images,” in *Proc. IEEE Conf. Comput. Vis. Pattern Recognit.*, 2016, pp. 2764–2772.
- [65] K. Zhang, W. Zuo, Y. Chen, D. Meng, and L. Zhang, “Beyond a Gaussian Denoiser: Residual learning of deep CNN for image denoising,” *IEEE Trans. Image Process.*, vol. 26, no. 7, pp. 3142–3155, Jul. 2017.
- [66] J. Yoo, S.-H. Lee, and N. Kwak, “Image restoration by estimating frequency distribution of local patches,” in *Proc. IEEE Conf. Comput. Vis. Pattern Recognit.*, 2018, pp. 6684–6692.
- [67] X. Fu, Z.-J. Zha, F. Wu, X. Ding, and J. Paisley, “JPEG artifacts via deep convolutional sparse coding,” in *Proc. IEEE Int. Conf. Comput. Vis.*, 2019, pp. 2501–2510.
- [68] J. Liu, D. Liu, W. Yang, S. Xia, X. Zhang, and Y. Dai, “A comprehensive benchmark for single image compression artifact reduction,” *IEEE Trans. Image Process.*, vol. 29, pp. 7845–7860, 2020.
- [69] Y. Chen and T. Pock, “Trainable nonlinear reaction diffusion: A flexible framework for fast and effective image restoration,” *IEEE Trans. Pattern Anal. Mach. Intell.*, vol. 39, no. 6, pp. 1256–1272, Jun. 2017.
- [70] H. Chang, M. K. Ng, and T. Zeng, “Reducing artifacts in jpeg decompression via a learned dictionary,” *IEEE Trans. Signal Process.*, vol. 62, no. 3, pp. 718–728, Feb. 2014.
- [71] C. Wang, J. Zhou, and S. Liu, “Adaptive non-local means filter for image deblocking,” *Signal Process., Image Commun.*, vol. 28, pp. 522–530, 2013.
- [72] Y. Zhang, K. Li, K. Li, B. Zhong, and Y. Fu, “Residual non-local attention networks for image restoration,” in *Proc. Int. Conf. Learn. Represent.*, 2019, pp. 1–18.
- [73] G. K. Wallace, “The JPEG still picture compression standard,” *IEEE Trans. Consum. Electron.*, vol. 38, no. 1, pp. 18–34, Feb. 1992.
- [74] K. Zhang, W. Zuo, and L. Zhang, “FFDNet: Toward a fast and flexible solution for CNN-based image denoising,” *IEEE Trans. Image Process.*, vol. 27, no. 9, pp. 4608–4622, Sep. 2018.
- [75] M. S. M. Sajjadi, R. Vemulapalli, and M. Brown, “Frame-recurrent video super-resolution,” in *Proc. IEEE Conf. Comput. Vis. Pattern Recognit.*, 2018, pp. 6626–6634.
- [76] E. Lesellier and J. Jung, “Robust wavelet-based arbitrary grid detection for MPEG,” in *Proc. IEEE Conf. Image Process.*, 2002, pp. 417–420.
- [77] K. He, X. Zhang, S. Ren, and J. Sun, “Identity mappings in deep residual networks,” in *Proc. Eur. Conf. Comput. Vis.*, 2016, pp. 630–645.
- [78] Y. Bengio, J. Louradour, R. Collobert, and M.-L. Alberi-Morel, “Curriculum learning,” in *Proc. Int. Conf. Mach. Learn.*, 2009, pp. 41–48.
- [79] D. Kingma and J. Ba, “Adam: A method for stochastic optimization,” in *Proc. Int. Conf. Learn. Represent.*, 2015, pp. 1–13.
- [80] Google Developers. (2010). *WebP - A New Image Format for the Web*. [Online]. Available: <https://developers.google.com/speed/webp/>
- [81] R. Timofte et al., “NTIRE 2017 challenge on single image super-resolution: methods and results,” in *Proc. IEEE Conf. Comput. Vis. Pattern Recognit. Workshops*, 2017, pp. 1110–1121.
- [82] R. Franzen. (2013). *Kodak Lossless True Color Image Suite*. [Online]. Available: <http://r0k.us/graphics/kodak/>
- [83] H. Luo, F. Zhou, G. Liao, and G. Qiu. (2021). *Online Materials for Super-resolving Compressed Images via Parallel and Series Integration of Artifact Reduction and Resolution Enhancement*. [Online]. Available: <http://www.vista.ac.cn/cisr-pcs/>
- [84] X. Liu, M. Tanaka, and M. Okutomi, “Single-image noise level estimation for blind denoising,” *IEEE Trans. Image Process.*, vol. 22, no. 12, pp. 5226–5237, Dec. 2013.
- [85] S. Liu, Q. Liao, J.-H. Xue, and F. Zhou, “Defocus map estimation from a single image using improved likelihood feature and edge-based basis,” *Pattern Recognit.*, vol. 107, pp. 1–17, Nov. 2020.
- [86] Z. Wang, A. C. Bovik, H. R. Sheikh, and E. P. Simoncelli, “Image quality assessment: from error visibility to structural similarity,” *IEEE Trans. Image Process.*, vol. 13, no. 4, pp. 600–612, Apr. 2004.
- [87] H. R. Sheikh, A. C. Bovik and G. de Veciana, “An information fidelity criterion for image quality assessment using natural scene statistics,” *IEEE Trans. Image Process.*, vol. 14, no. 12, pp. 2117–2128, Dec. 2005.
- [88] F. Zhou, R. Yao, B. Liu, and G. Qiu, “Visual quality assessment for super-resolved images: Database and method,” *IEEE Trans. Image Process.*, vol. 28, no. 7, pp. 3528–3541, Jul. 2019.

Hongming Luo is now a Doctor candidate in the College of Information Engineering, Shenzhen University, China. His researches focus on image super-resolution and restoration.

Fei Zhou received the B.Eng. degree in electronics and information engineering from the Huazhong University of Science and Technology, in 2007, and the Ph.D. degree in electronic engineering, Tsinghua University, in 2013. From 2013 to 2016, he was a post-doctoral fellow with the Graduate School at Shenzhen, Tsinghua University. From 2017 to 2018, he was a visiting scholar with the Department of Statistical Science, University College London. He is currently an Assistant Professor with the College of Information Engineering, Shenzhen University. He has authored over 50 papers internationally. His research interests include image super-resolution, image interpolation, image quality assessment, etc. He is a reviewer of many reputable journals, including IEEE Transactions on Image processing, IEEE Transactions on Multimedia, Information Sciences, etc. He also serves as a guest editor of Neurocomputing and Signal Processing: Image Communication.

Guangsen Liao is now a Master in the College of Information Engineering, Shenzhen University, China. His researches focus on image enhancement and image processing.

Guoping Qiu is a Distinguished Professor of Information Engineering, Director of Shenzhen University Intelligent Robotics Centre at Shenzhen University, China, and a Chair Professor of Visual Information Processing at the University of Nottingham, Nottingham, UK. He has taught in universities in the UK and Hong Kong and also consulted for multinational companies in Europe, Hong Kong and China. His research interests include image processing, pattern recognition, and machine learning. He is particularly known for his pioneering research in high dynamic range imaging and machine learning based image processing technologies. He has published widely and holds several European and US patents. Technologies developed in his lab have laid the cornerstone for successful spinout companies who are developing advanced digital photography software enjoyed by tens of millions of global users.

Supplementary Materials

This PDF file is a copy of our online supplementary materials at <http://www.vista.ac.cn/cisr-pcs/>. We provide this off-line file to avoid a slow on-line loading when you wish to review our online materials.

1. Dataset

We collect 76 uncompressed images by ourselves to supplement Kodak24(<http://r0k.us/graphics/kodak/>). These images are selected from 1000 images with size of 3840×2160 and cropped as images with size of 600×600 . They are from a variety of scenarios including indoors, outdoors and so on. We prepare these data using MATLAB.

We take these 100 images as our testing data for our all experiments.

Download dataset links: <http://www.vista.ac.cn/download/ucd76/>

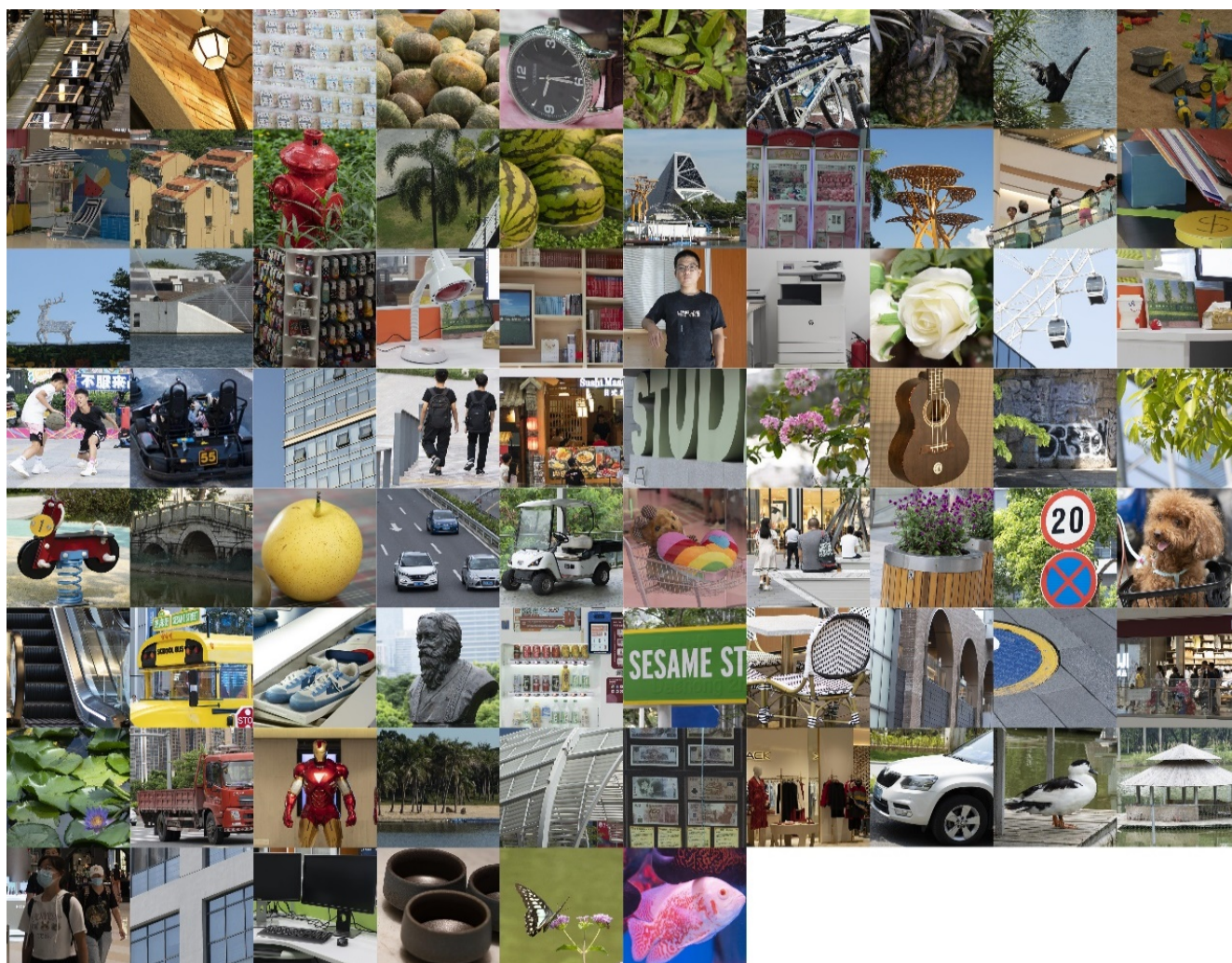


Fig.1 Thumbnail of our collected images

2. Comparisons for Super-resolution

We prepare dataset by two steps: 1) Bicubic down-sampling by MATLAB *imresize*. 2) Compressing down-sampled images by MATLAB *imwrite* for JPEG or OPENCV *imwrite* for WebP.

Up-scaling factor: 2, 3, 4 JPEG quality factors (QFs): 10, 20, 30, 40, 50 WebP QFs: 5, 10, 20, 30, 40

Involved methods: CISRDCNN [1], ICSD [2], DnCNN [3], Aplus [4], EDSR [5], RCAN [6], SAN [7], USRNet [8], NRIBP [9]. The best two performances are **bold** in the following tables.

2.1 Quantitative Comparisons

2.1.1 Quantitative Comparisons for Different Scaling Factors and Compression Configurations Based on PSNR

Up-scaling factor	SR Models	QFs										
		JPEG & 10	JPEG & 20	JPEG & 30	JPEG & 40	JPEG & 50	WebP & 5	WebP & 10	WebP & 20	WebP & 30	WebP & 40	Average
2	CISRDCNN	27.51	28.91	29.62	30.07	30.41	27.88	28.57	29.45	30.07	30.54	29.31
	ICSD	26.96	28.31	29.02	29.52	29.90	27.47	28.19	29.11	29.76	30.30	28.86
	DnCNN + Aplus	27.67	29.09	29.84	30.31	30.66	27.71	28.43	29.39	30.09	30.65	29.39
	DnCNN + EDSR	27.68	29.13	29.91	30.42	30.82	27.72	28.46	29.48	30.27	30.92	29.48
	DnCNN + RCAN	27.35	28.49	29.04	29.38	29.63	27.36	27.93	28.67	29.21	29.64	28.67
	DnCNN + SAN	27.68	29.14	29.91	30.41	30.82	27.72	28.46	29.48	30.27	30.92	29.48
	DnCNN + USRNet	27.68	29.12	29.90	30.42	30.82	27.74	28.48	29.51	30.28	30.93	29.49
	USRNet	27.23	28.41	28.93	29.20	29.38	27.60	28.09	28.69	29.05	29.28	28.59
	Aplus + NRIBP	27.43	28.82	29.54	30.00	30.34	27.56	28.25	29.17	29.85	30.38	29.13
	EDSR + NRIBP	27.57	29.06	29.86	30.39	30.80	27.71	28.45	29.48	30.28	30.93	29.46
	RCAN + NRIBP	27.46	28.78	29.45	29.88	30.19	27.52	28.18	29.04	29.68	30.20	29.03
	USRNet+ NRIBP	27.57	29.05	29.87	30.40	30.81	27.73	28.47	29.52	30.30	30.96	29.47
	Our tiny model	28.01	29.51	30.31	30.84	31.25	28.41	29.11	30.07	30.81	31.41	29.97
	Our full model	28.11	29.61	30.43	30.95	31.37	28.56	29.26	30.20	30.93	31.53	30.10
3	CISRDCNN	25.90	27.05	27.62	27.98	28.22	26.27	26.84	27.53	28.00	28.36	27.37
	ICSD	25.35	26.41	26.94	27.31	27.58	25.82	26.41	27.02	27.49	27.88	26.82
	DnCNN + Aplus	25.97	27.08	27.64	28.00	28.25	26.08	26.67	27.41	27.93	28.34	27.34
	DnCNN + EDSR	25.97	27.08	27.68	28.06	28.35	26.08	26.69	27.49	28.09	28.56	27.40
	DnCNN + RCAN	25.70	26.59	27.02	27.26	27.45	25.74	26.20	26.78	27.19	27.51	26.75
	DnCNN + SAN	25.97	27.09	27.67	28.06	28.34	26.09	26.69	27.49	28.08	28.55	27.40
	DnCNN + USRNet	25.96	27.09	27.68	28.08	28.37	26.09	26.72	27.53	28.13	28.61	27.43
	USRNet	25.59	26.63	27.09	27.35	27.52	26.03	26.48	27.02	27.33	27.55	26.86
	Aplus + NRIBP	25.70	26.78	27.32	27.66	27.91	25.88	26.44	27.15	27.64	28.02	27.05
	EDSR + NRIBP	25.88	27.02	27.64	28.04	28.33	26.07	26.68	27.48	28.09	28.57	27.38
	RCAN + NRIBP	25.78	26.80	27.31	27.62	27.85	25.89	26.41	27.08	27.55	27.93	27.02
	USRNet+ NRIBP	25.87	27.03	27.65	28.05	28.36	26.08	26.70	27.53	28.13	28.62	27.40
	Our tiny model	26.22	27.43	28.08	28.49	28.78	26.65	27.23	27.98	28.54	28.99	27.84
	Our full model	26.31	27.53	28.18	28.59	28.88	26.78	27.35	28.09	28.63	29.07	27.94
4	CISRDCNN	24.73	25.70	26.17	26.46	26.66	25.09	25.56	26.14	26.53	26.81	25.99
	ICSD	24.29	25.20	25.65	25.97	26.19	24.75	25.12	25.73	26.11	26.45	25.54
	DnCNN + Aplus	24.87	25.86	26.33	26.63	26.85	25.02	25.53	26.18	26.62	26.96	26.09
	DnCNN + EDSR	24.88	25.87	26.37	26.70	26.94	25.03	25.55	26.27	26.78	27.18	26.16
	DnCNN + RCAN	24.68	25.50	25.87	26.10	26.27	24.75	25.17	25.71	26.06	26.34	25.65
	DnCNN + SAN	24.88	25.87	26.37	26.70	26.94	25.04	25.56	26.27	26.78	27.17	26.16
	DnCNN + USRNet	24.87	25.87	26.39	26.72	26.97	25.05	25.59	26.31	26.83	27.23	26.18
	USRNet	24.48	25.40	25.81	26.05	26.21	24.95	25.35	25.82	26.09	26.28	25.65
	Aplus + NRIBP	24.63	25.58	26.04	26.32	26.53	24.82	25.31	25.92	26.34	26.66	25.81
	EDSR + NRIBP	24.81	25.82	26.34	26.68	26.93	25.03	25.55	26.27	26.79	27.18	26.14
	RCAN + NRIBP	24.74	25.64	26.08	26.35	26.55	24.88	25.34	25.93	26.34	26.66	25.85
	USRNet+ NRIBP	24.81	25.83	26.36	26.70	26.96	25.04	25.58	26.30	26.83	27.23	26.16
	Our tiny model	25.12	26.21	26.76	27.11	27.36	25.53	26.03	26.71	27.19	27.56	26.55
	Our full model	25.17	26.25	26.81	27.17	27.44	25.62	26.13	26.78	27.25	27.62	26.62

2.1.2 Quantitative Comparisons for Different Scaling Factors and Compression Configurations Based on SSIM

Up-scaling factor	SR Models	QFs										
		JPEG & 10	JPEG & 20	JPEG & 30	JPEG & 40	JPEG & 50	WebP & 5	WebP & 10	WebP & 20	WebP & 30	WebP & 40	Average
2	CISRDCNN	0.7459	0.7910	0.8131	0.8262	0.8361	0.7558	0.7785	0.8068	0.8260	0.8399	0.8019
	ICSD	0.7306	0.7755	0.7989	0.8143	0.8262	0.7392	0.7644	0.7971	0.8199	0.8368	0.7903
	DnCNN + Aplus	0.7476	0.7924	0.8149	0.8286	0.8390	0.7476	0.7715	0.8024	0.8237	0.8392	0.8007
	DnCNN + EDSR	0.7484	0.7935	0.8165	0.8309	0.8418	0.7485	0.7729	0.8048	0.8273	0.8438	0.8028
	DnCNN + RCAN	0.7430	0.7853	0.8063	0.8192	0.8288	0.7426	0.7649	0.7939	0.8141	0.8290	0.7927
	DnCNN + SAN	0.7484	0.7935	0.8165	0.8308	0.8417	0.7485	0.7729	0.8047	0.8272	0.8436	0.8027
	DnCNN + USRNet	0.7481	0.7933	0.8164	0.8308	0.8416	0.7486	0.7731	0.8050	0.8273	0.8436	0.8028
	USRNet	0.7303	0.7667	0.7806	0.7877	0.7921	0.7362	0.7515	0.7698	0.7802	0.7864	0.7682
	Aplus + NRIBP	0.7441	0.7905	0.8137	0.8279	0.8385	0.7473	0.7713	0.8023	0.8237	0.8393	0.7999
	EDSR + NRIBP	0.7449	0.7918	0.8155	0.8303	0.8414	0.7483	0.7728	0.8048	0.8273	0.8439	0.8021
	RCAN + NRIBP	0.7411	0.7855	0.8077	0.8214	0.8315	0.7423	0.7654	0.7954	0.8165	0.8322	0.7939
	USRNet+ NRIBP	0.7449	0.7914	0.8153	0.8300	0.8412	0.7480	0.7727	0.8048	0.8273	0.8437	0.8020
	Our tiny model	0.7590	0.8031	0.8254	0.8391	0.8492	0.7697	0.7914	0.8192	0.8392	0.8540	0.8149
	Our full model	0.7621	0.8058	0.8284	0.8424	0.8523	0.7740	0.7953	0.8225	0.8420	0.8567	0.8181
3	CISRDCNN	0.6887	0.7262	0.7454	0.7572	0.7659	0.7034	0.7224	0.7459	0.7618	0.7738	0.7391
	ICSD	0.6716	0.7081	0.7278	0.7413	0.7518	0.6903	0.7108	0.7358	0.7533	0.7678	0.7259
	DnCNN + Aplus	0.6890	0.7252	0.7443	0.7564	0.7655	0.6950	0.7150	0.7407	0.7586	0.7723	0.7362
	DnCNN + EDSR	0.6892	0.7257	0.7454	0.7583	0.7682	0.6959	0.7167	0.7438	0.7633	0.7783	0.7385
	DnCNN + RCAN	0.6818	0.7146	0.7319	0.7430	0.7513	0.6866	0.7046	0.7281	0.7447	0.7577	0.7245
	DnCNN + SAN	0.6893	0.7256	0.7454	0.7583	0.7681	0.6959	0.7166	0.7437	0.7631	0.7779	0.7384
	DnCNN + USRNet	0.6892	0.7259	0.7458	0.7588	0.7689	0.6965	0.7175	0.7450	0.7646	0.7795	0.7392
	USRNet	0.6724	0.7080	0.7236	0.7324	0.7380	0.6892	0.7037	0.7212	0.7316	0.7384	0.7159
	Aplus + NRIBP	0.6846	0.7225	0.7425	0.7552	0.7648	0.6943	0.7144	0.7404	0.7584	0.7721	0.7349
	EDSR + NRIBP	0.6853	0.7234	0.7441	0.7575	0.7677	0.6956	0.7164	0.7438	0.7634	0.7784	0.7376
	RCAN + NRIBP	0.6805	0.7153	0.7336	0.7453	0.7540	0.6870	0.7057	0.7301	0.7474	0.7609	0.7260
	USRNet+ NRIBP	0.6853	0.7234	0.7441	0.7576	0.7680	0.6954	0.7165	0.7443	0.7640	0.7791	0.7378
	Our tiny model	0.7025	0.7395	0.7598	0.7726	0.7817	0.7167	0.7355	0.7599	0.7773	0.7909	0.7536
	Our full model	0.7048	0.7421	0.7623	0.7749	0.7842	0.7205	0.7389	0.7628	0.7798	0.7931	0.7564
4	CISRDCNN	0.6534	0.6835	0.6994	0.7092	0.7166	0.6687	0.6838	0.7030	0.7161	0.7256	0.6959
	ICSD	0.6353	0.6648	0.6809	0.6924	0.7017	0.6584	0.6696	0.6919	0.7066	0.7191	0.6820
	DnCNN + Aplus	0.6517	0.6812	0.6973	0.7075	0.7155	0.6606	0.6767	0.6981	0.7131	0.7244	0.6926
	DnCNN + EDSR	0.6522	0.6819	0.6986	0.7096	0.7186	0.6619	0.6789	0.7020	0.7188	0.7318	0.6954
	DnCNN + RCAN	0.6446	0.6705	0.6851	0.6943	0.7016	0.6518	0.6660	0.6853	0.6991	0.7096	0.6808
	DnCNN + SAN	0.6523	0.6820	0.6987	0.7097	0.7185	0.6621	0.6789	0.7020	0.7186	0.7314	0.6954
	DnCNN + USRNet	0.6522	0.6822	0.6993	0.7106	0.7195	0.6628	0.6800	0.7035	0.7204	0.7332	0.6964
	USRNet	0.6345	0.6648	0.6795	0.6879	0.6939	0.6558	0.6680	0.6833	0.6924	0.6987	0.6759
	Aplus + NRIBP	0.6471	0.6781	0.6950	0.7058	0.7142	0.6594	0.6756	0.6973	0.7125	0.7238	0.6909
	EDSR + NRIBP	0.6486	0.6798	0.6973	0.7088	0.7181	0.6616	0.6786	0.7020	0.7188	0.7318	0.6946
	RCAN + NRIBP	0.6437	0.6711	0.6862	0.6959	0.7036	0.6523	0.6670	0.6870	0.7014	0.7125	0.6821
	USRNet+ NRIBP	0.6486	0.6798	0.6976	0.7093	0.7187	0.6616	0.6789	0.7027	0.7198	0.7328	0.6950
	Our tiny model	0.6652	0.6976	0.7155	0.7268	0.7352	0.6816	0.6973	0.7185	0.7341	0.7457	0.7117
	Our full model	0.6669	0.6993	0.7172	0.7284	0.7372	0.6845	0.7000	0.7207	0.7359	0.7475	0.7138

2.1.3 Quantitative Comparisons for Different Scaling Factors and Compression Configurations Based on IFC

Up-scaling factor	SR Models	QFs										
		JPEG & 10	JPEG & 20	JPEG & 30	JPEG & 40	JPEG & 50	WebP & 5	WebP & 10	WebP & 20	WebP & 30	WebP & 40	Average
2	CISRDCNN	1.1926	1.7447	2.1072	2.3625	2.5733	1.2821	1.4986	1.8196	2.0827	2.3012	1.8965
	ICSD	1.1035	1.6262	1.9665	2.2213	2.4447	1.2044	1.4123	1.7331	2.0102	2.2458	1.7968
	DnCNN + Aplus	1.1944	1.7263	2.0853	2.3504	2.5800	1.1549	1.3647	1.6903	1.9706	2.2103	1.8327
	DnCNN + EDSR	1.2152	1.7647	2.1405	2.4213	2.6667	1.1750	1.3909	1.7308	2.0277	2.2863	1.8819
	DnCNN + RCAN	1.1685	1.6573	1.9708	2.1912	2.3742	1.1212	1.3131	1.6058	1.8534	2.0606	1.7316
	DnCNN + SAN	1.2154	1.7647	2.1400	2.4206	2.6658	1.1747	1.3906	1.7302	2.0270	2.2854	1.8814
	DnCNN + USRNet	1.2162	1.7653	2.1404	2.4214	2.6665	1.1793	1.3962	1.7376	2.0346	2.2923	1.8850
	USRNet	1.1369	1.6118	1.8577	1.9998	2.0932	1.2434	1.4162	1.6440	1.8007	1.9068	1.6710
	Aplus + NRIBP	1.1642	1.7163	2.0890	2.3640	2.6015	1.1595	1.3717	1.7026	1.9871	2.2308	1.8387
	EDSR + NRIBP	1.1721	1.7333	2.1149	2.3993	2.6468	1.1679	1.3837	1.7242	2.0218	2.2802	1.8644
	RCAN + NRIBP	1.1470	1.6689	2.0185	2.2741	2.4922	1.1211	1.3199	1.6282	1.8947	2.1242	1.7689
	USRNet+ NRIBP	1.1718	1.7287	2.1080	2.3916	2.6379	1.1661	1.3826	1.7256	2.0235	2.2826	1.8618
	Our tiny model	1.3514	1.9263	2.3192	2.6046	2.8498	1.4383	1.6633	2.0002	2.2891	2.5365	2.0979
	Our full model	1.3897	1.9736	2.3708	2.6630	2.9147	1.4902	1.7183	2.0573	2.3475	2.5963	2.1521
3	CISRDCNN	0.7826	1.1248	1.3458	1.5025	1.6311	0.8644	1.0097	1.2208	1.3910	1.5326	1.2405
	ICSD	0.7130	1.0229	1.2213	1.3725	1.5028	0.8090	0.9442	1.1023	1.2622	1.4123	1.1363
	DnCNN + Aplus	0.7793	1.0955	1.3056	1.4598	1.5935	0.7667	0.9076	1.1187	1.2976	1.4529	1.1777
	DnCNN + EDSR	0.7932	1.1203	1.3421	1.5085	1.6542	0.7829	0.9304	1.1549	1.3506	1.5221	1.2159
	DnCNN + RCAN	0.7500	1.0337	1.2132	1.3415	1.4462	0.7291	0.8524	1.0350	1.1866	1.3168	1.0905
	DnCNN + SAN	0.7933	1.1205	1.3418	1.5076	1.6529	0.7832	0.9300	1.1537	1.3487	1.5189	1.2151
	DnCNN + USRNet	0.7942	1.1224	1.3442	1.5117	1.6583	0.7873	0.9352	1.1628	1.3603	1.5314	1.2208
	USRNet	0.7283	1.0496	1.2322	1.3477	1.4295	0.8434	0.9736	1.1496	1.2733	1.3600	1.1387
	Aplus + NRIBP	0.7552	1.0864	1.3054	1.4670	1.6063	0.7682	0.9108	1.1261	1.3088	1.4668	1.1801
	EDSR + NRIBP	0.7614	1.0978	1.3235	1.4928	1.6403	0.7765	0.9236	1.1489	1.3455	1.5166	1.2027
	RCAN + NRIBP	0.7333	1.0337	1.2308	1.3764	1.5001	0.7268	0.8539	1.0457	1.2086	1.3510	1.1060
	USRNet+ NRIBP	0.7609	1.0960	1.3207	1.4902	1.6366	0.7752	0.9226	1.1506	1.3485	1.5201	1.2021
	Our tiny model	0.8993	1.2620	1.5040	1.6811	1.8305	0.9824	1.1374	1.3676	1.5588	1.7241	1.3947
	Our full model	0.9270	1.2975	1.5446	1.7233	1.8749	1.0245	1.1815	1.4130	1.6027	1.7666	1.4356
4	CISRDCNN	0.5808	0.8143	0.9628	1.0647	1.1499	0.6447	0.7470	0.8985	1.0168	1.1155	0.8995
	ICSD	0.5135	0.7226	0.8535	0.9530	1.0384	0.5889	0.6311	0.7795	0.8938	1.0000	0.7974
	DnCNN + Aplus	0.5656	0.7809	0.9223	1.0234	1.1098	0.5632	0.6625	0.8141	0.9393	1.0475	0.8429
	DnCNN + EDSR	0.5788	0.8016	0.9518	1.0619	1.1581	0.5799	0.6846	0.8496	0.9894	1.1121	0.8768
	DnCNN + RCAN	0.5444	0.7360	0.8580	0.9417	1.0122	0.5363	0.6218	0.7496	0.8552	0.9444	0.7800
	DnCNN + SAN	0.5801	0.8026	0.9529	1.0622	1.1578	0.5806	0.6849	0.8487	0.9874	1.1091	0.8766
	DnCNN + USRNet	0.5785	0.8026	0.9543	1.0654	1.1624	0.5831	0.6889	0.8560	0.9980	1.1215	0.8811
	USRNet	0.5169	0.7354	0.8661	0.9479	1.0095	0.6151	0.7096	0.8410	0.9322	1.0017	0.8175
	Aplus + NRIBP	0.5491	0.7746	0.9220	1.0277	1.1182	0.5642	0.6647	0.8190	0.9467	1.0569	0.8443
	EDSR + NRIBP	0.5548	0.7846	0.9376	1.0497	1.1470	0.5742	0.6790	0.8442	0.9844	1.1074	0.8663
	RCAN + NRIBP	0.5307	0.7317	0.8621	0.9562	1.0368	0.5329	0.6210	0.7552	0.8684	0.9658	0.7861
	USRNet+ NRIBP	0.5542	0.7833	0.9367	1.0490	1.1467	0.5744	0.6793	0.8462	0.9884	1.1120	0.8670
	Our tiny model	0.6639	0.9247	1.0949	1.2164	1.3201	0.7361	0.8511	1.0203	1.1599	1.2792	1.0267
	Our full model	0.6780	0.9427	1.1171	1.2403	1.3478	0.7597	0.8761	1.0470	1.1882	1.3068	1.0504

2.1.4 Quantitative Comparisons for Different Scaling Factors and Compression Configurations Based on SIS

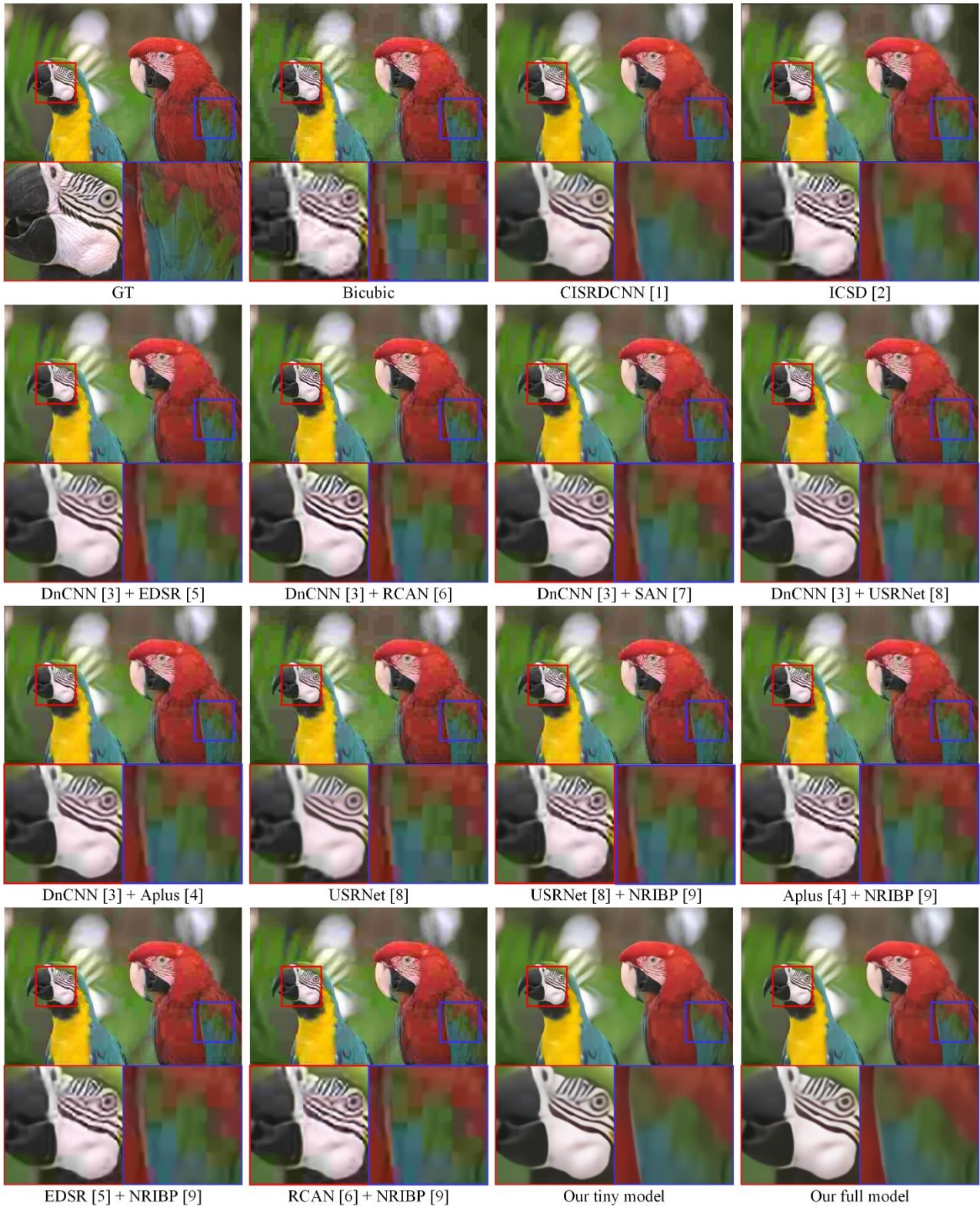
Up-scaling factor	SR Models	QFs										
		JPEG & 10	JPEG & 20	JPEG & 30	JPEG & 40	JPEG & 50	WebP & 5	WebP & 10	WebP & 20	WebP & 30	WebP & 40	Average
2	CISRDCNN	0.5550	0.6892	0.7496	0.7830	0.8062	0.5679	0.6411	0.7235	0.7728	0.8058	0.7094
	ICSD	0.5169	0.6405	0.7100	0.7507	0.7801	0.4940	0.5759	0.6756	0.7375	0.7804	0.6662
	DnCNN + Aplus	0.5844	0.7094	0.7648	0.7940	0.8147	0.5556	0.6286	0.7135	0.7672	0.8025	0.7135
	DnCNN + EDSR	0.5818	0.7170	0.7767	0.8093	0.8324	0.5528	0.6307	0.7238	0.7814	0.8200	0.7226
	DnCNN + RCAN	0.6351	0.7512	0.7995	0.8248	0.8427	0.6094	0.6792	0.7580	0.8049	0.8351	0.7540
	DnCNN + SAN	0.5819	0.7168	0.7766	0.8091	0.8324	0.5525	0.6300	0.7230	0.7807	0.8197	0.7223
	DnCNN + USRNet	0.5804	0.7146	0.7744	0.8072	0.8302	0.5532	0.6305	0.7230	0.7802	0.8187	0.7212
	USRNet	0.5476	0.6362	0.6757	0.6951	0.7070	0.5323	0.5829	0.6399	0.6725	0.6922	0.6381
	Aplus + NRIBP	0.5639	0.6924	0.7508	0.7827	0.8048	0.5470	0.6204	0.7065	0.7593	0.7944	0.7022
	EDSR + NRIBP	0.5736	0.7114	0.7739	0.8081	0.8320	0.5527	0.6308	0.7242	0.7820	0.8208	0.7210
	RCAN + NRIBP	0.5989	0.7246	0.7800	0.8102	0.8311	0.5832	0.6547	0.7382	0.7895	0.8235	0.7334
	USRNet+ NRIBP	0.5748	0.7113	0.7732	0.8074	0.8312	0.5560	0.6330	0.7252	0.7826	0.8212	0.7216
	Our tiny model	0.6020	0.7299	0.7863	0.8178	0.8394	0.6253	0.6874	0.7602	0.8069	0.8398	0.7495
	Our full model	0.6118	0.7373	0.7941	0.8256	0.8461	0.6367	0.6981	0.7685	0.8129	0.8449	0.7576
3	CISRDCNN	0.3654	0.4803	0.5442	0.5844	0.6146	0.4140	0.4786	0.5565	0.6063	0.6427	0.5287
	ICSD	0.3295	0.4332	0.5048	0.5533	0.5906	0.3503	0.4216	0.5353	0.5962	0.6406	0.4955
	DnCNN + Aplus	0.3875	0.5013	0.5612	0.5987	0.6263	0.4068	0.4735	0.5551	0.6081	0.6477	0.5366
	DnCNN + EDSR	0.3729	0.4955	0.5625	0.6052	0.6379	0.3985	0.4697	0.5603	0.6217	0.6672	0.5391
	DnCNN + RCAN	0.4367	0.5523	0.6103	0.6455	0.6709	0.4554	0.5228	0.6044	0.6552	0.6913	0.5845
	DnCNN + SAN	0.3717	0.4944	0.5615	0.6040	0.6370	0.3960	0.4668	0.5581	0.6191	0.6651	0.5374
	DnCNN + USRNet	0.3741	0.4951	0.5614	0.6043	0.6373	0.4012	0.4723	0.5627	0.6229	0.6678	0.5399
	USRNet	0.3554	0.4347	0.4788	0.5052	0.5243	0.3855	0.4286	0.4817	0.5115	0.5312	0.4637
	Aplus + NRIBP	0.3634	0.4736	0.5348	0.5730	0.6010	0.3926	0.4568	0.5356	0.5865	0.6239	0.5141
	EDSR + NRIBP	0.3654	0.4883	0.5585	0.6034	0.6370	0.3983	0.4697	0.5608	0.6222	0.6677	0.5371
	RCAN + NRIBP	0.3904	0.5037	0.5664	0.6049	0.6335	0.4261	0.4918	0.5726	0.6241	0.6618	0.5475
	USRNet+ NRIBP	0.3672	0.4889	0.5585	0.6034	0.6370	0.4053	0.4755	0.5651	0.6259	0.6702	0.5397
	Our tiny model	0.4194	0.5391	0.6052	0.6459	0.6751	0.4692	0.5318	0.6101	0.6636	0.7045	0.5864
	Our full model	0.4189	0.5419	0.6087	0.6490	0.6789	0.4750	0.5360	0.6131	0.6654	0.7063	0.5893
4	CISRDCNN	0.2462	0.3224	0.3695	0.3996	0.4223	0.2994	0.3418	0.3966	0.4332	0.4604	0.3691
	ICSD	0.2265	0.2975	0.3545	0.3958	0.4271	0.2724	0.3523	0.4153	0.4627	0.4975	0.3702
	DnCNN + Aplus	0.2698	0.3539	0.4022	0.4339	0.4576	0.3102	0.3580	0.4206	0.4623	0.4942	0.3963
	DnCNN + EDSR	0.2400	0.3281	0.3827	0.4210	0.4498	0.2934	0.3460	0.4182	0.4678	0.5080	0.3855
	DnCNN + RCAN	0.2840	0.3715	0.4203	0.4515	0.4758	0.3331	0.3825	0.4452	0.4858	0.5170	0.4167
	DnCNN + SAN	0.2406	0.3289	0.3833	0.4209	0.4497	0.2920	0.3434	0.4151	0.4648	0.5044	0.3843
	DnCNN + USRNet	0.2420	0.3294	0.3843	0.4220	0.4509	0.2934	0.3465	0.4182	0.4681	0.5082	0.3863
	USRNet	0.2406	0.2913	0.3246	0.3465	0.3619	0.2816	0.3083	0.3457	0.3666	0.3836	0.3251
	Aplus + NRIBP	0.2483	0.3258	0.3738	0.4049	0.4279	0.2928	0.3378	0.3957	0.4338	0.4629	0.3704
	EDSR + NRIBP	0.2369	0.3239	0.3806	0.4204	0.4498	0.2934	0.3464	0.4189	0.4686	0.5087	0.3847
	RCAN + NRIBP	0.2553	0.3364	0.3860	0.4193	0.4447	0.3150	0.3619	0.4224	0.4624	0.4934	0.3897
	USRNet+ NRIBP	0.2387	0.3257	0.3825	0.4224	0.4516	0.3004	0.3521	0.4237	0.4730	0.5127	0.3883
	Our tiny model	0.2861	0.3845	0.4434	0.4815	0.5091	0.3532	0.4021	0.4681	0.5185	0.5579	0.4404
	Our full model	0.2876	0.3856	0.4457	0.4842	0.5122	0.3539	0.4024	0.4692	0.5192	0.5579	0.4418

2.2 Visual Comparisons (compression type & quality factor & scale)

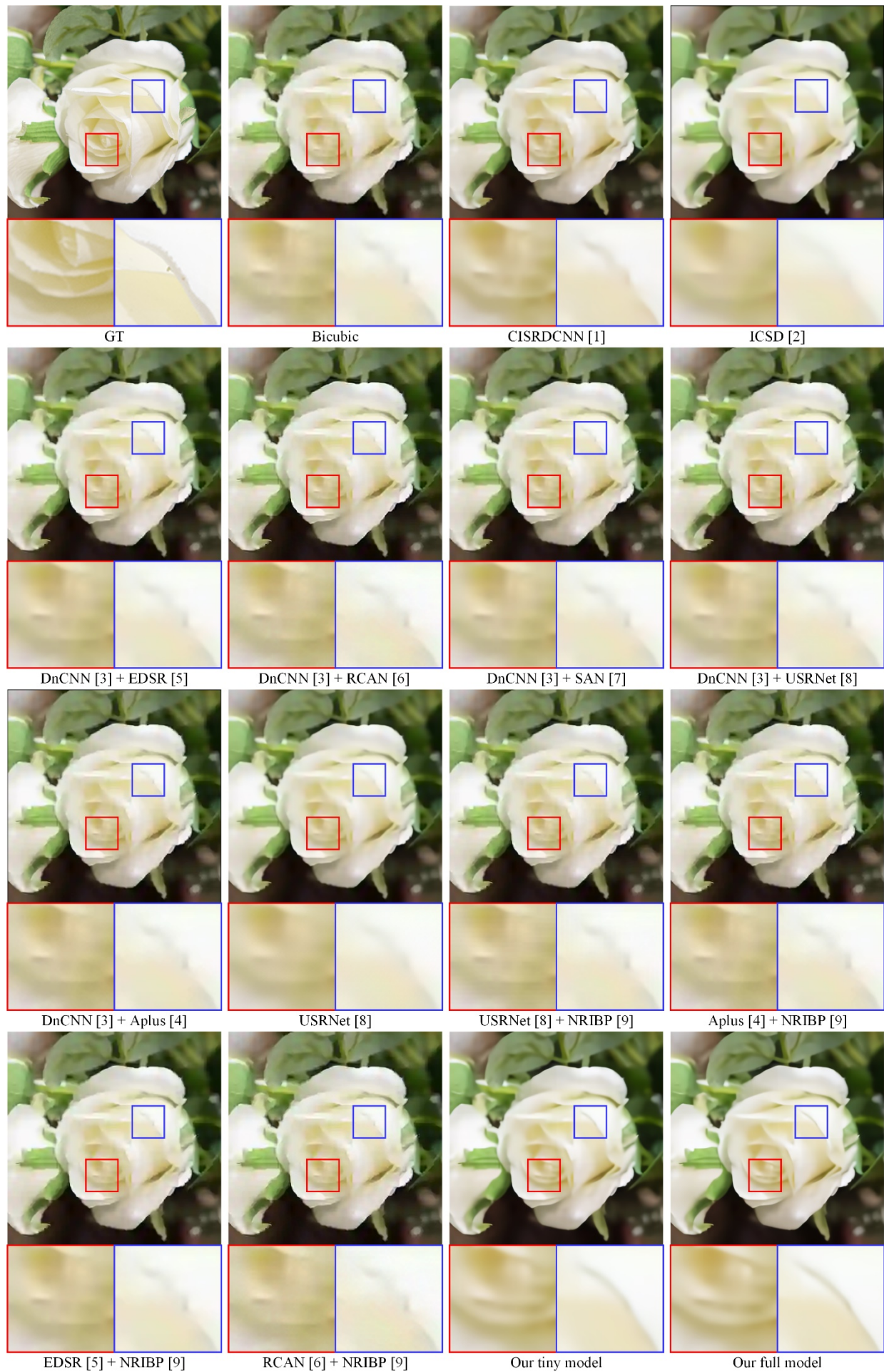
2.2.1 JPEG & 10 & $\times 2$



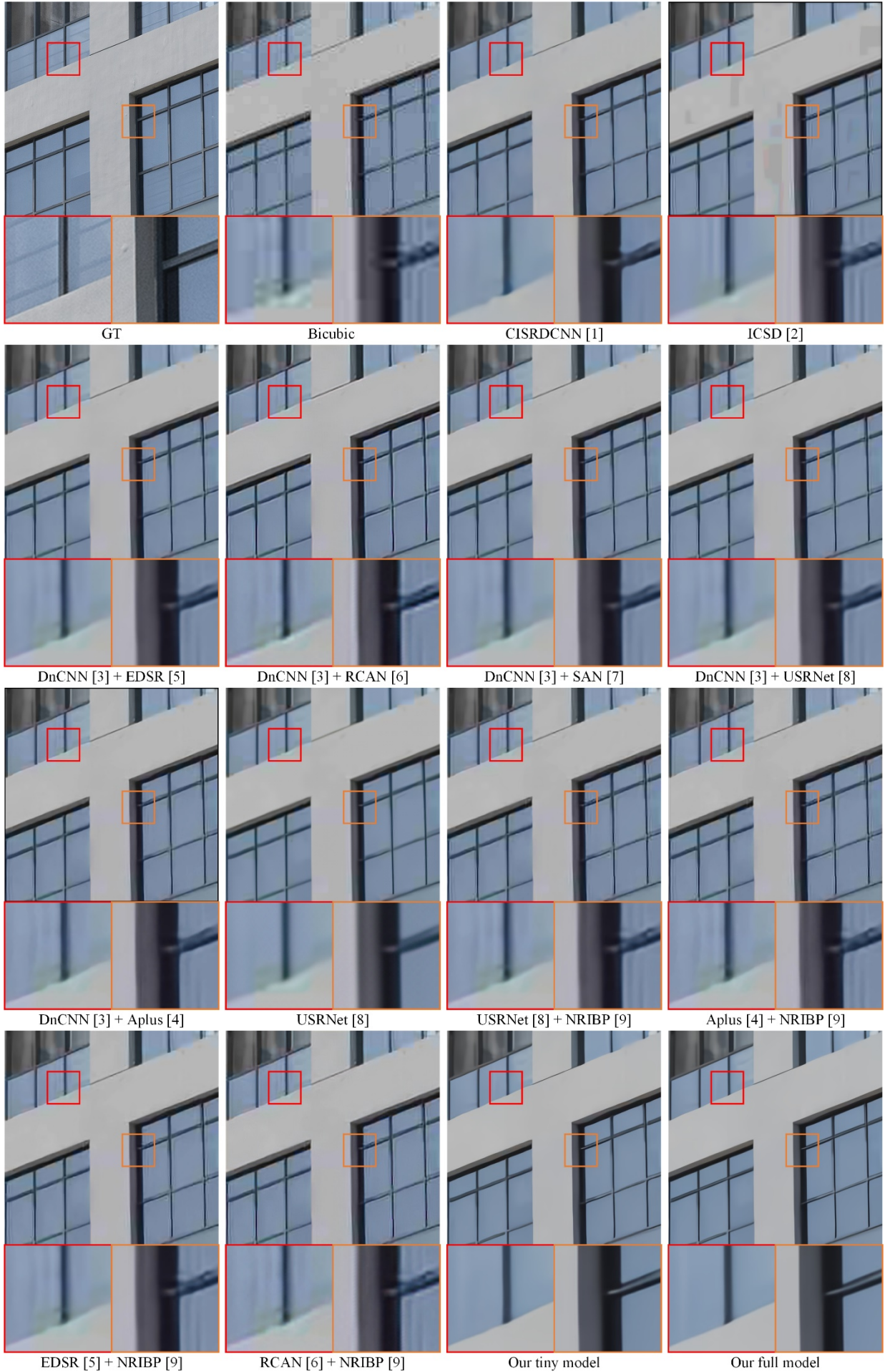
2.2.2 JPEG & 10 & $\times 2$



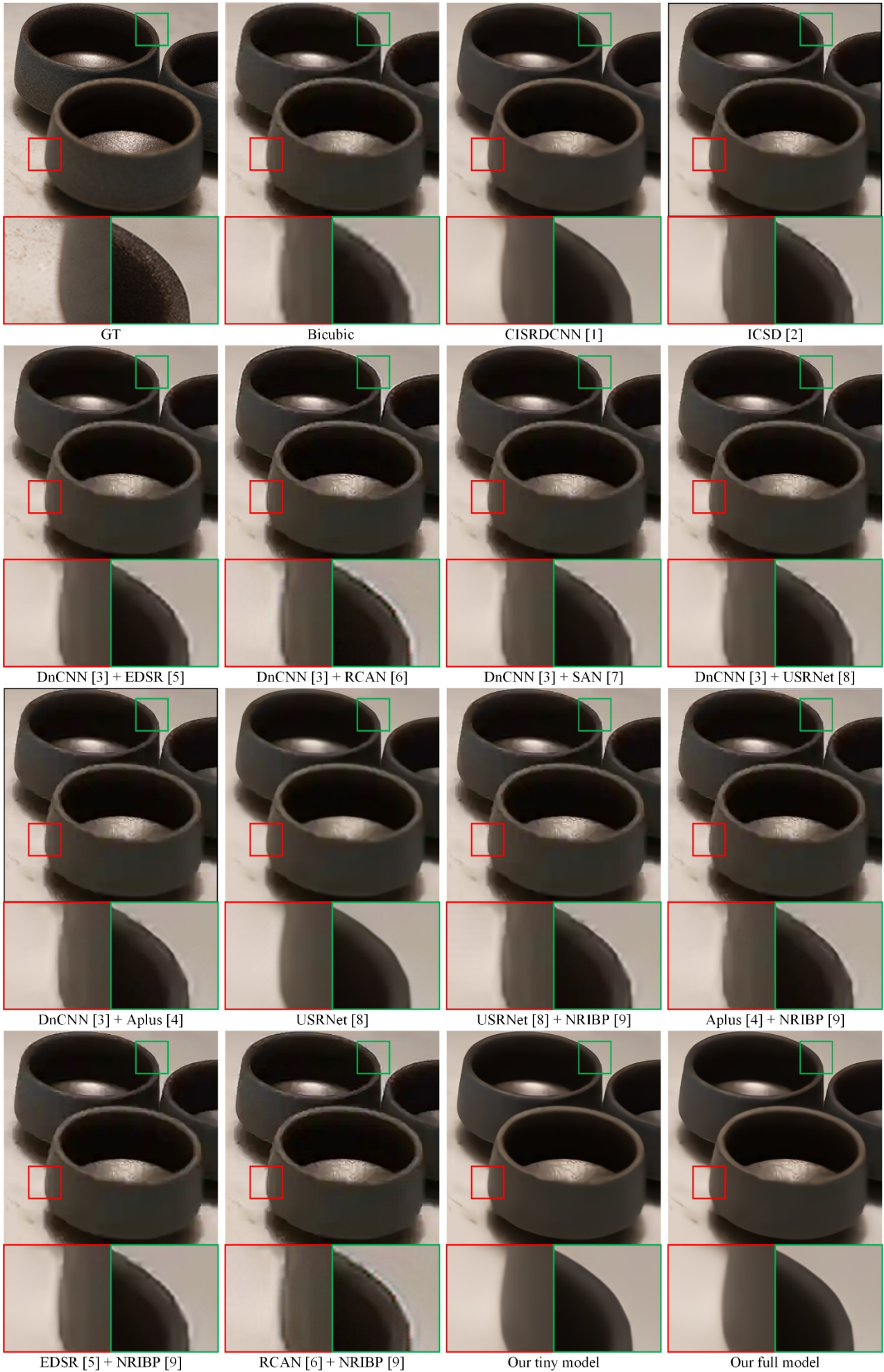
2.2.3 WebP & 5 & ×2



2.2.4 JPEG & 20 & $\times 3$



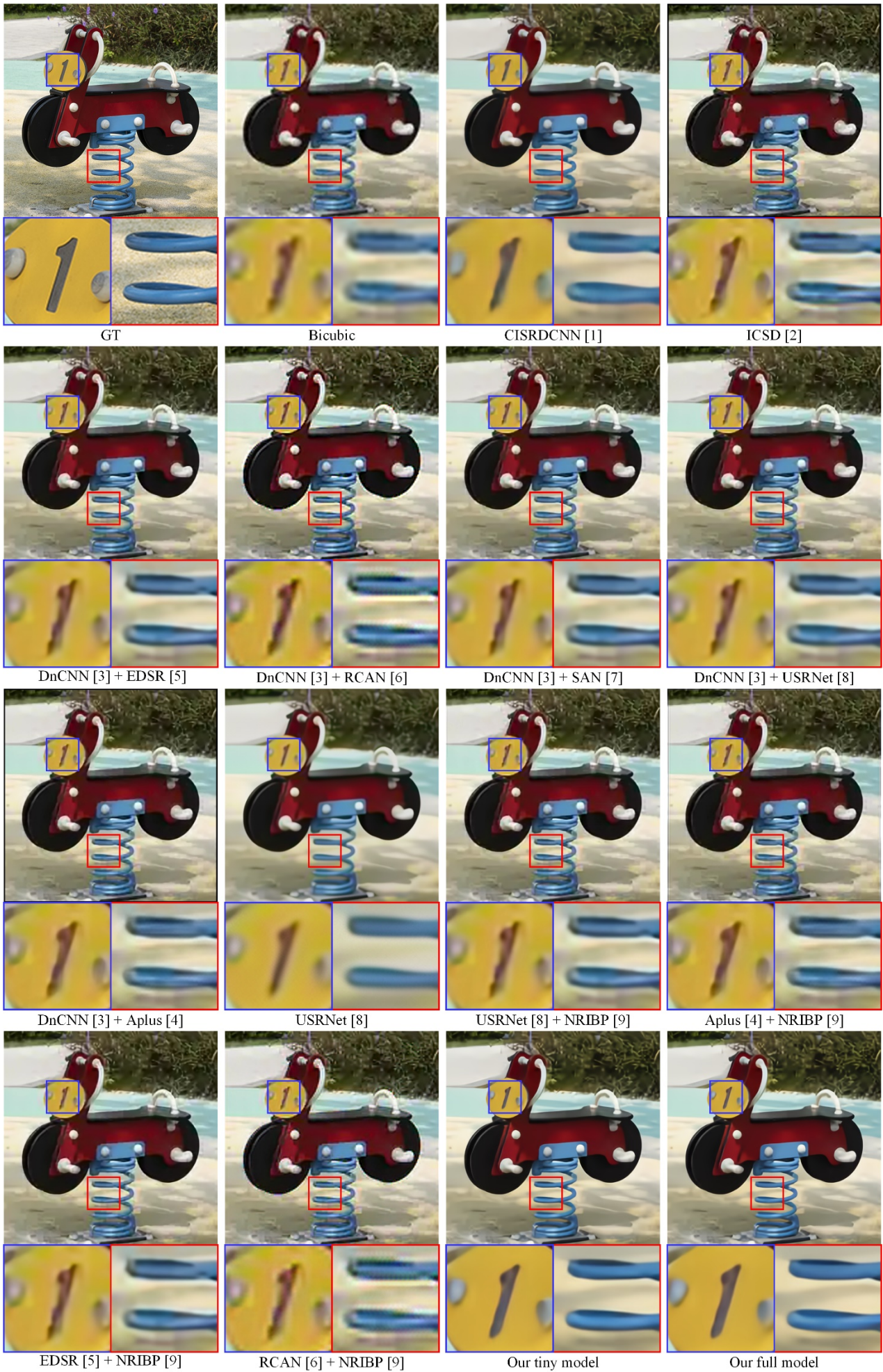
2.2.5 WebP & 20 & ×3



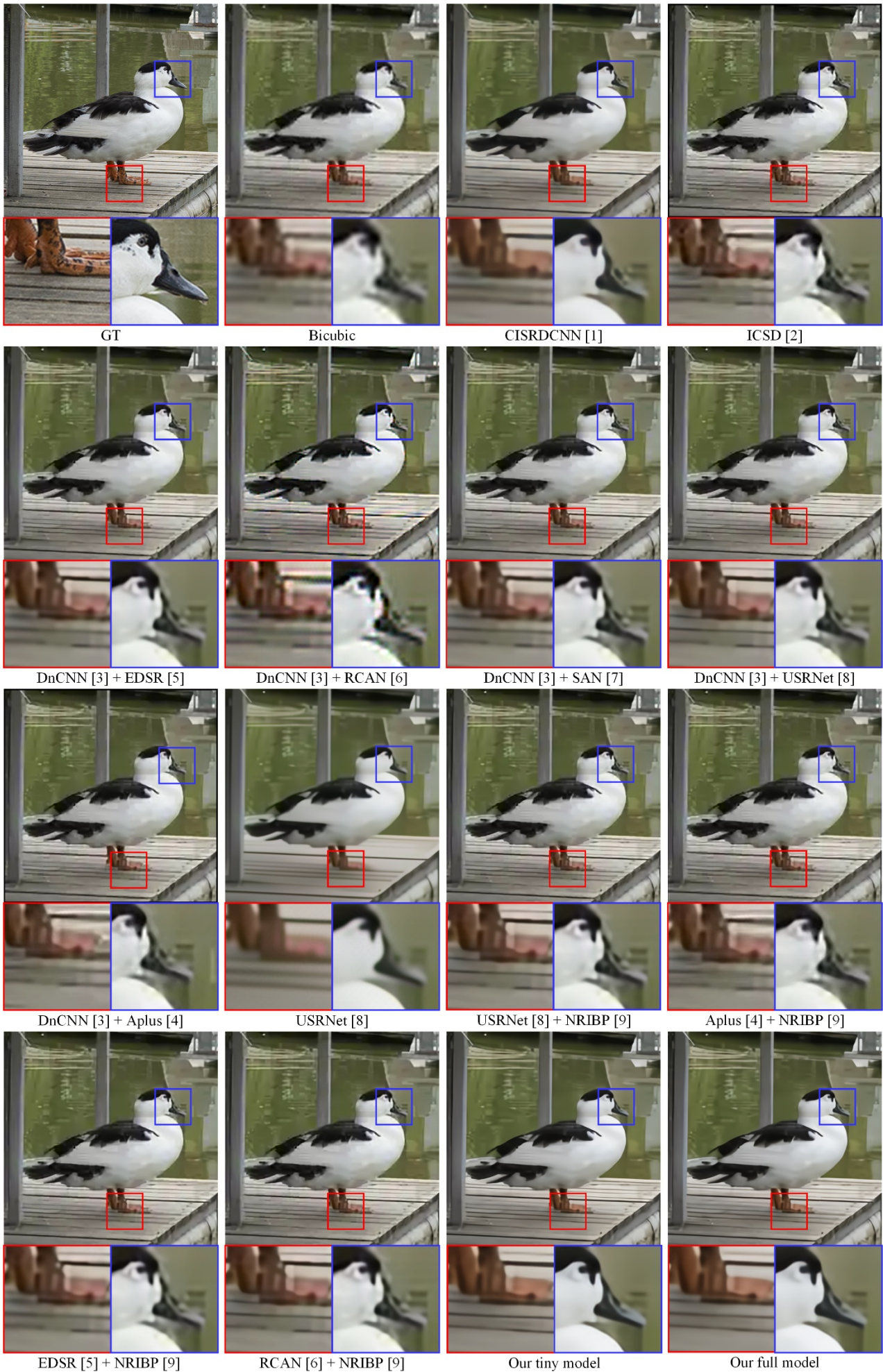
2.2.6 WebP & 30 & ×3



2.2.7 WebP & 40 & ×4



2.2.8 WebP & 40 & ×4



3. Comparisons for Compression Artifacts Reduction

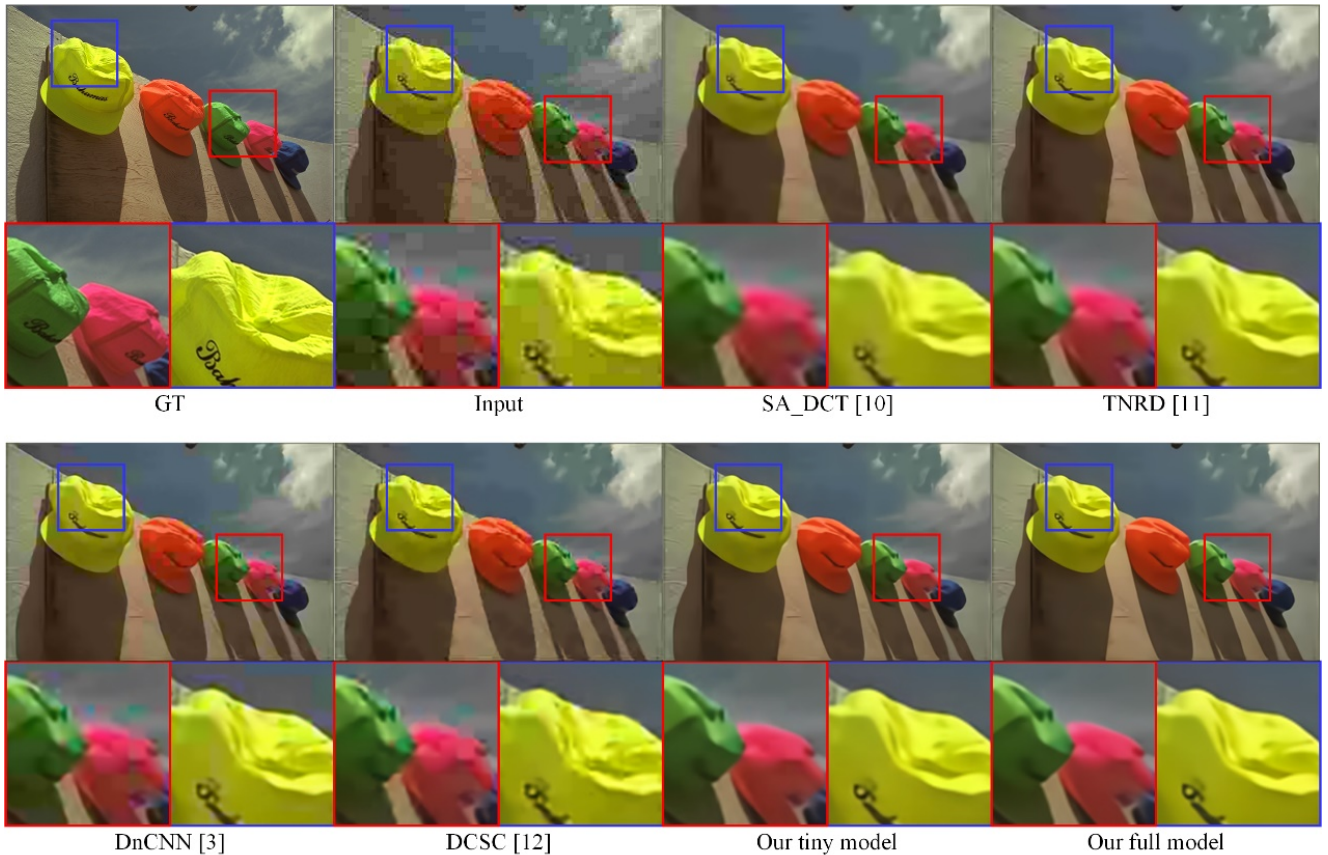
Involved methods: SA_DCT [10], TNRD [11], DnCNN [3], DCSC [12]. Among these compared methods, the inputs of SA_DCT and TNRD are limited to JPEG images. Thus, they are not able to restore WebP images. The best two performances are **bold** in the following tables.

3.1 Quantitative Comparisons

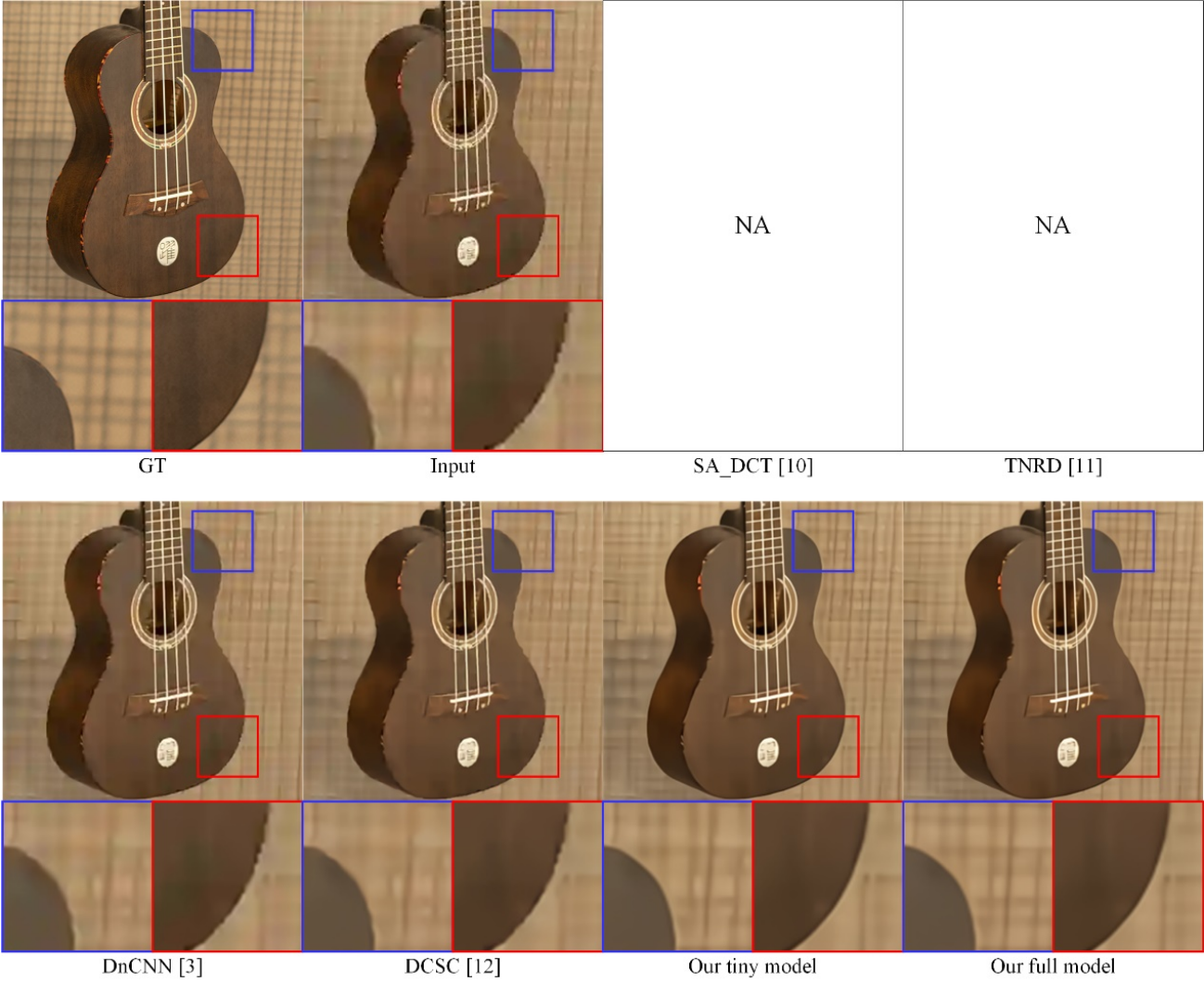
Method	Metric	Compression type & quality factor										Average
		JPEG & 10	JPEG & 20	JPEG & 30	JPEG & 40	JPEG & 50	WebP & 5	WebP & 10	WebP & 20	WebP & 30	WebP & 40	
SA_DCT	PSNR	29.20	31.40	32.73	33.68	34.48	--	--	--	--	--	32.25
TNRD		29.92	32.30	33.74	34.60	35.35	--	--	--	--	--	33.19
DnCNN		29.95	32.41	33.84	34.83	35.65	30.01	31.15	32.80	34.15	35.36	33.03
DCSC		29.48	32.06	33.52	34.52	35.31	30.15	31.29	32.90	34.18	35.27	32.87
Our tiny model		30.32	32.84	34.82	35.34	36.16	30.81	31.91	33.48	34.77	35.95	33.66
Our full model		30.46	33.00	34.50	35.54	36.38	31.02	32.12	33.69	34.98	36.16	33.87
SA_DCT	SSIM	0.8295	0.8881	0.9142	0.9291	0.9396	--	--	--	--	--	0.9059
TNRD		0.8494	0.9038	0.9272	0.9386	0.9469	--	--	--	--	--	0.9188
DnCNN		0.8522	0.9072	0.9301	0.9425	0.9510	0.8455	0.8748	0.9084	0.9293	0.9433	0.9140
DCSC		0.8423	0.9024	0.9264	0.9390	0.9477	0.8469	0.8756	0.9084	0.9284	0.9417	0.9115
Our tiny model		0.8603	0.9126	0.9345	0.9462	0.9541	0.8655	0.8900	0.9183	0.9363	0.9487	0.9226
Our full model		0.8633	0.9148	0.9363	0.9479	0.9557	0.8695	0.8934	0.9209	0.9384	0.9504	0.9251

3.2 Visual Comparisons (compression type & quality factor)

3.2.1 JPEG & 10



3.2.2 WebP & 10

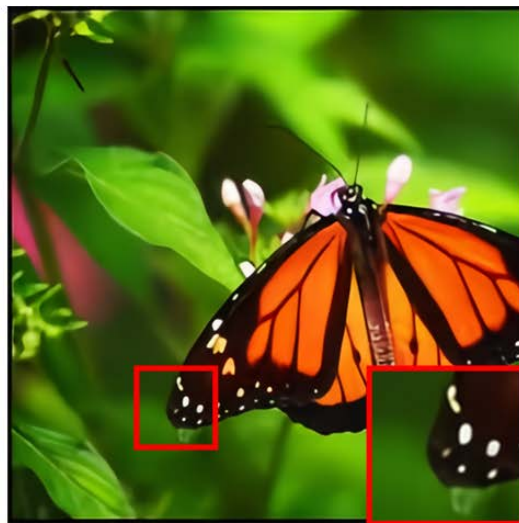


4. Super-resolving Real-world compressed images

4.1 JPEG



Bicubic



Our full model

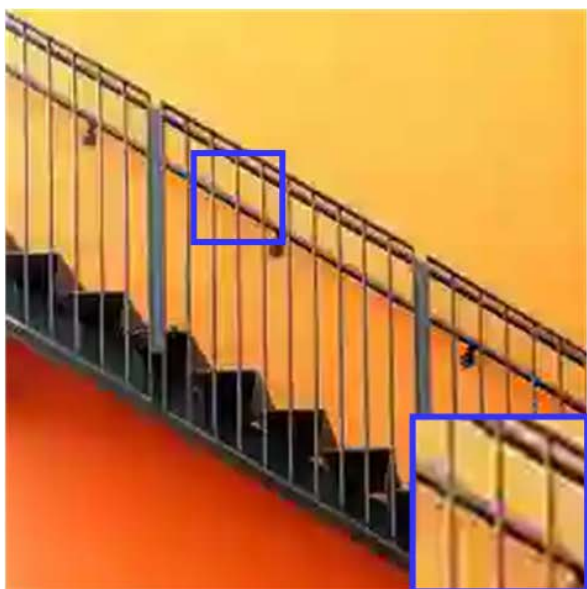


Bicubic

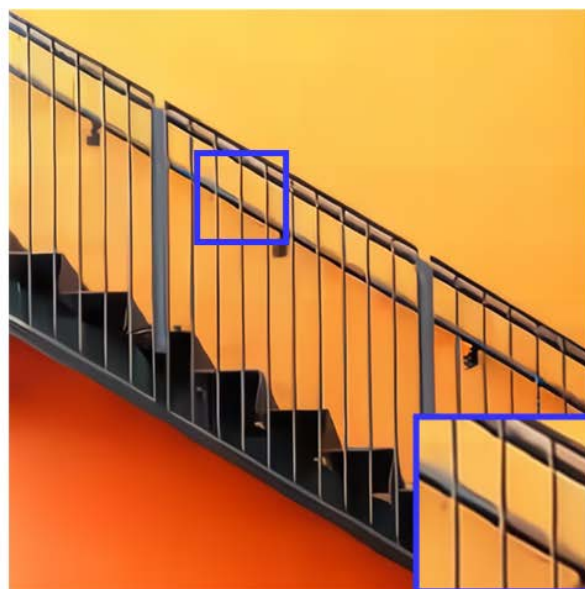


Our full model

4.2 WebP



Bicubic



Our full model

5. Each Time Step Results



6. Other Information

All of our results are available at:

Baidu drive link: https://pan.baidu.com/s/1eF41V3jnQnR_1CwuD1PYkA password: 1xuj

Google drive link: https://drive.google.com/drive/folders/13oJ1lb-GuAM1OEg6QiXV_gHJ3_y9vlzS

Code link: https://github.com/luohongming/CISR_PSI

Reference:

- [1] T. Li, X. He, L. Qing, Q. Teng, and H. Chen, "An iterative framework of cascaded deblocking and superresolution for compressed images," IEEE Trans. Multimedia, vol. 20, no. 6, pp. 1305–1320, Jun. 2018.
- [2] H. Chen, X. He, C. Ren, L. Qing, and Q. Teng, "CISRDCNN: Super-resolution of compressed images using deep convolutional neural networks," Neurocomputing, vol. 285, pp. 204–219, 2018.
- [3] K. Zhang, W. Zuo, Y. Chen, D. Meng, and L. Zhang, "Beyond a Gaussian Denoiser: Residual learning of deep CNN for image denoising," IEEE Trans. Image Process., vol. 26, no. 7, pp. 3142–3155, Jul. 2017.
- [4] Timofte, V. De, and L. Van Gool, "A+: Adjusted anchored neighborhood regression for fast super-resolution," in Proc. IEEE Asian Conf. Comput. Vis., 2014, pp. 111–126.
- [5] Lim, S. Son, H. Kim, S. Nah, and K. M. Lee, "Enhanced deep residual networks for single image super-resolution," in Proc. IEEE Conf. Comput. Vis. Pattern Recognit. Workshops, 2017, pp. 1132–1140.
- [6] Y. Zhang, K. Li, K. Li, L. Wang, B. Zhong, and Y. Fu, "Image super-resolution using very deep residual channel attention networks," in Proc. Eur. Conf. Comput. Vis., 2018, pp. 294–310.
- [7] T. Dai, J. Cai, Y. Zhang, S-T. Xia, and L. Zhang, "Second-order attention network for single image super-resolution," in Proc. IEEE Conf. Comput. Vis. Pattern Recognit., 2019, pp. 11057–11066.
- [8] K. Zhang, L. V. Gool, and R. Timofte, "Deep unfolding network for image super-resolution," in Proc. IEEE Conf. Comput. Vis. Pattern Recognit., 2020, pp. 3217–3226.
- [9] J.-S. Yoo and J.-O. Kim, "Nosie-robust iterative back-projection," IEEE Trans. Image Process., vo. 29, pp. 1219–1232, 2020.
- [10] Foi, V. Katkovnik, and K. Egiazarian, "Pointwise shape-adaptive DCT for high-quality denoising and deblocking of grayscale and color images," IEEE Trans. Image Process., vol. 16, no. 5, pp. 1395–1411, May 2007.
- [11] Chen and T. Pock, "Trainable nonlinear reaction diffusion: A flexible framework for fast and effective image restoration," IEEE Trans. Pattern Anal. Mach. Intell., vol. 39, no. 6, pp. 1256–1272, Jun. 2017.
- [12] Fu, Z.-J. Zha, F. Wu, X. Ding, and J. Paisley, "JPEG artifacts via deep convolutional sparse coding," in Proc. IEEE Int. Conf. Comput. Vis., 2019, pp. 2501–2510.